REPORT DOCUMENTATION PAGE		*Form Approved*
		OMB No. 0704-0188

The public reporting burden for this collection of information is estimated to average 1 hour per response, including the time for reviewing instructions, searching existing data sources, gathering and maintaining the data needed, and completing and reviewing the collection of information. Send comments regarding this burden estimate or any other aspect of this collection of information, including suggestions for reducing the burden, to Department of Defense, Washington Headquarters Services, Directorate for Information Operations and Reports (0704-0188), 1215 Jefferson Davis Highway, Suite 1204, Arlington, VA 22202-4302. Respondents should be aware that notwithstanding any other provision of law, no person shall be subject to any penalty for failing to comply with a collection of information if it does not display a currently valid OMB control number.
PLEASE DO NOT RETURN YOUR FORM TO THE ABOVE ADDRESS.

1. REPORT DATE *(DD-MM-YYYY)* 20-12-2014	2. REPORT TYPE Final	3. DATES COVERED *(From - To)* 25 Mar 2013 to 24 Sep 2014

4. TITLE AND SUBTITLE High-temperature superconductivity in diamond films - from fundamentals to device applications	5a. CONTRACT NUMBER FA2386-13-1-4055
	5b. GRANT NUMBER Grant AOARD-134055
	5c. PROGRAM ELEMENT NUMBER 61102F
6. AUTHOR(S) Prof Steven Prawer	5d. PROJECT NUMBER
	5e. TASK NUMBER
	5f. WORK UNIT NUMBER

7. PERFORMING ORGANIZATION NAME(S) AND ADDRESS(ES) University of Melbourne Corner Swanston St. and Tin Alley Parkville, VIC Australia	8. PERFORMING ORGANIZATION REPORT NUMBER N/A

9. SPONSORING/MONITORING AGENCY NAME(S) AND ADDRESS(ES) AOARD UNIT 45002 APO AP 96338-5002	10. SPONSOR/MONITOR'S ACRONYM(S) AFRL/AFOSR/IOA(AOARD)
	11. SPONSOR/MONITOR'S REPORT NUMBER(S) AOARD-134055

12. DISTRIBUTION/AVAILABILITY STATEMENT

   Distribution Code A: Approved for public release; distribution is unlimited.

13. SUPPLEMENTARY NOTES

14. ABSTRACT
The specific aims of the research (as proposed in the original grant application) are:
(i) to test the hypotheses that repeated implants of boron in diamond below the graphitization limit (followed by high-temperature annealing) can increase the carrier density in the buried layer to levels required for the occurrence of superconductivity; (ii) the demonstration of superconductivity in a (repeatedly) boron-implanted and annealed diamond crystal in our dilution refrigerator, after which; (iii) we will implement a superconducting quantum interference device (SQUID).
The ultimate goal of the work is to develop the technology and expertise to create robust, superconducting devices in diamond that can operate in high-magnetic fields and relatively high temperatures ($Tc \gg 11$ K according to the theory of M.L. Cohen for a fractional boron concentration of 30%), c.f. Fig. 1. Further benefits of this research may be found in the high-frequency operation of such devices in environmentally harsh environments such as space. The work presented here is essentially a feasibility study for the existence of high-Tc diamond superconductors based on B-implantation followed by new techniques for the annealing of damage.

15. SUBJECT TERMS

   Superconducting Materials, diamond films

16. SECURITY CLASSIFICATION OF:			17. LIMITATION OF ABSTRACT	18. NUMBER OF PAGES	19a. NAME OF RESPONSIBLE PERSON Ingrid J. Wysong, Ph.D.
a. REPORT	b. ABSTRACT	c. THIS PAGE			
U	U	U	SAR	49	19b. TELEPHONE NUMBER *(Include area code)* +81-42-511-2000

Standard Form 298 (Rev. 8/98)
Prescribed by ANSI Std. Z39.18

Final Report for AOARD Grant 134055

"**High-temperature superconductivity in diamond films -
from fundamentals to device applications**"

November 20th, 2014

Name of Principal Investigators (PI and Co-PIs):

Steven Prawer, Laurens Willems van Beveren, and Marvin Cohen
- e-mail address : s.prawer@unimelb.edu.au
- Institution : The University of Melbourne
- Mailing Address : School of Physics, Parkville VIC 3010, Australia
- Phone : +61 3 8344 5460
- Fax : +61 3 9347 4783

Period of Performance: 25 Mar 2013 – 24 Sep 2014

Abstract:

The specific aims of the research (as proposed in the original grant application) are:

(i)   to test the hypotheses that repeated implants of boron in diamond below the graphitization limit (followed by high-temperature annealing) can increase the carrier density in the buried layer to levels required for the occurrence of superconductivity;

(ii)   the demonstration of superconductivity in a (repeatedly) boron-implanted and annealed diamond crystal in our dilution refrigerator, after which;

(iii)   we will implement a superconducting quantum interference device (SQUID).

The ultimate goal of the work is to develop the technology and expertise to create robust, superconducting devices in diamond that can operate in high-magnetic fields and relatively high temperatures ($T_c \gg 11$ K according to the theory of M.L. Cohen for a fractional boron concentration of 30%), c.f. Fig. 1. Further benefits of this research may be found in the high-frequency operation of such devices in environmentally harsh environments such as space. The work presented here is essentially a feasibility study for the existence of high-T_c diamond superconductors based on B-implantation followed by new techniques for the annealing of damage.

In pursuit of these goals we have investigated the feasibility of ion implanting diamond plates with boron to create highly conducting, sub-surface layers. These layers hold great promise for the emergence of superconductivity at relatively high temperatures provided the carrier density can be made high enough and the crystal damage is minimized through high-temperature annealing techniques. The short-term goal of is to show that the critical temperature of boron-doped diamond increases with hole concentration. To this end we have developed and refined experimental protocols to fabricate such samples and analyze their crystal integrity using Raman spectroscopy. We have also developed the software and equipment to electronically characterize buried layers as a function of both temperature and magnetic field.

In particular, we have:

- implanted 2 MeV boron (B) ions into type-IIa diamond plates (followed by high temperature annealing to repair crystal damage) to create heavily doped and highly conducting layers (*p*-type) buried in the diamond matrix.
- refined the parameters of the ion-implantation technique to avoid graphitization (using both simulation tools and Raman spectroscopy analysis).
- developed a technique to make low-resistance electrical contacts to these buried layers using a laser cutter in combination with active braise alloying. The latter is essential in order to investigate the superconducting properties of this material in our cryogen-free dilution refrigerator.
- performed low-temperature (4-5 K) electronic characterization of helium (He) implanted (and high-temperature annealed) diamond material to investigate the as-obtained resistivity of buried graphitic material.
- commenced Hall measurements in the van der Pauw geometry to investigate the magneto-resistance of the material and extract parameters such as carrier density and mobility.
- presented several pathways towards increasing the concentration of B in diamond crystals in order to observe a superconducting transition.

Introduction:

Highly boron-doped regions in diamond show great promise in high-temperature superconducting device applications. Typically, this material is grown by a high-pressure, high-temperature process (HPHT) or by a microwave-assisted CVD technique where boron is added to the reactor in the gas phase. In this work, we explore the possibility of creating a high-temperature superconductor by boron-implantation into diamond films. To this end our goal is to create a buried layer of highly doped diamond, whose carrier density is close to or above the metal-insulator-transition, with minimal lattice imperfections. Key to achieving superconductivity in these buried layers is to understand what determines the electronic transport and minimize lattice imperfections after implantation by high-temperature annealing techniques.
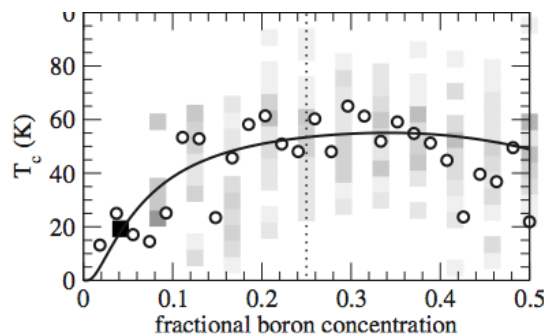

Fig 1. Theoretically predicted critical temperature as a function of boron concentration. Most experimental data so far has only been taken in the 0 to 0.1 regime. A T_c of 55 K for 0.3 fractional boron concentration is predicted, provided crystal integrity can be maintained. From reference [1].

An overview of experimentally obtained values of the critical temperature as a function of boron density is shown in Fig. 2. There is a trend visible that for higher values of boron doping the critical temperature increases, in agreement with the theoretical prediction above.
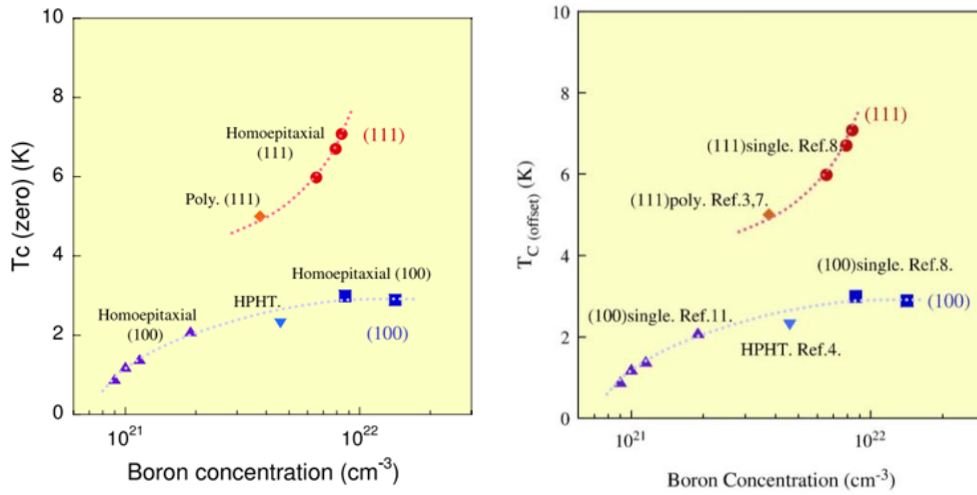
Fig 2. Experimental data showing critical temperature as a function of boron concentration. From references in [2].

However, this cannot be the complete story, as the crystal quality will play an important role shaping the electronic landscape of the material. For instance, the metal-insulator-transition (MIT) value reported in the literature varies by an order of magnitude with one paper reporting an MIT of $\sim 4 \times 10^{21}/cm^3$ for a B-implanted single crystal diamond epilayers grown by CVD (100) [3] and a more recent work reporting a value of $\sim 3.9 \times 10^{20}/cm^3$ [4]. This difference is most likely related to the details of the crystal integrity in the material, which can be analyzed with Raman spectroscopy and cross-sectional transmission electron microscopy (X-TEM) and X-ray crystallography [5].

Experiment:

[1] 2 MeV ion implantation:

Dr. Jeffrey McCallum implanted initially two 3x3x0.3 mm CVD-grown diamond plates at the Australian National University (ANU). The ion-implantation process of boron in diamond was performed at an ion-energy of 2 MeV with a fluence of 2 and 5×10^{15} B/cm². The actual implantation took place under liquid nitrogen conditions (LN₂) and was followed by a rapid anneal to 500°C for 10 min under either forming gas anneal or argon gas directly after implantation. This procedure is known as the Cold Implant Rapid Anneal (CIRA) process and was used to maximize boron activation. This process freezes in the vacancies formed during implantation before they become mobile and diffuse away. Typical beam currents used were 0.5-1 μA and 50 nA during the scanning of the beam over the surface. The B-implanted diamond plates appear brownish after implantation, which due to the vacancies formed in the material. Later, hot-implants (400-600°C) at higher fluence were investigated.
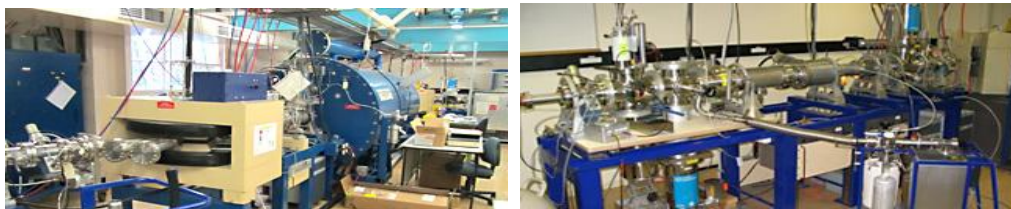

Fig 3. (left) Deep MeV implanter at the ANU. (right) Target chamber at the end of the beam line. The CVD plates were kept at liquid N₂ temperatures during implantation.

As a test sample, a buried graphitic sample was fabricated (for use in the low-temperature measurements and testing the electrical contacts) by RT helium (He) implantation above the critical dose using one of the 3 beamlines at the University of Melbourne's Pelletron implanter. The energy for this implant used was 1.789 MeV at a fluence of 5×10^{16} He/cm^2 corresponding to an end of range of ~3.8 μm below the surface. Details of this procedure can be found in reference [5].

[2] High-temperature annealing:

High temperature annealing of the implanted diamond plates was performed using the electron beam of a Thermionics metal evaporator. The vacuum in this system could be maintained to 5×10^{-5} mbar throughout the annealing of 10-15 minutes at typical temperatures of 1500°C. Placing the diamond plates in a specially designed graphite crucible prevented contamination of the sample from the surroundings. Temperature feedback was possible using a calibrated pyrometer with an accuracy of about 25°C. In principle, much longer anneals in time are possible in this system. It is essential to keep the electron beam sweeping over the graphite crucible to distribute the heat generated. If not, a hole is easily burned into the crucible and the sample will be compromised (this happened once).

Fig 4. High temperature annealing of the diamond plate inside the Thermionics evaporator (left). Graphite box used for annealing mounted in the hearth of the e-gun evaporator (right).

In Fig. 4 we can see a picture of the graphite crucible used for the HTA process. The e-beam hits the bottom plate of the crucible and heats up the box in a uniform fashion. The box has a side lid that is kept closed during the process. However, residual gas from the sidewalls of the vacuum system could still enter the box and start the graphitization process. In the future, a dedicated annealing system (no evaporation of metals and dielectrics) will be used to avoid graphitization of diamond samples.

[3] Raman spectroscopy:

The incident laser light interacts with the matter through the phonons and the reflected light is analyzed with a grating to monitor the Raman frequency shift of the light. The sensitivity of the Raman technique depends on the optical cross section, which is wavelength dependent. This is an excellent technique to analyze the diamond crystal integrity and look for the presence of graphitic material arising from the processing. It allows for the observation of damage peaks after implantation.

Fig 5. Renishaw InVia Reflex Raman spectrometer used to take the 532 nm Raman spectra presented. An infrared laser source was also used to avoid photoluminescence signals.

The Raman spectra in this work were taken using both infrared (IR) (1064 nm) and visible Raman spectrometers (514 and 532 nm) currently available in the School. The most convenient visible Raman spectrometer is the InVia Renishaw system with both 532 (visible) and 1064 nm (IR) laser sources. We have also looked at the diamond plates with near UV (325 nm) light, but the optics is tricky to setup correctly as compared to the InVia setup. Typical laser powers used are 1% of a 10 mW source, with microscope objectives of 20x – 100x that correspond to a micrometer spot size. Different depths of focus of these objectives allow probing either the bulk crystal or investigating near-surface effects. The advantage of the IR laser source is that it does not excite the nitrogen-vacancy centers in the diamond material and therefore a detailed examination of the defect peaks (e.g. the G peak) can be performed (waveshift <2000 /cm) not hindered by a photoluminescence (PL) background, which obscures these peaks. High numerical aperture objectives were used for defect studies (n/a = 0.75).

[4] Laser milling:

In order to make electrical contact with the buried B doped layers, we used a Laser Micro Cutting System (Alpha) from Oxford Lasers to mill holes into the diamond plates. We used a typical laser power of 3-5%, which cuts holes deeper than 3.8 μm, which is more than sufficient to make contact with the B doped layers which are buried 1-2 μm below the surface. In order to start the laser cutting into the diamond plate it is essential to first gold (Au) coat the surface to avoid chipping of the implanted area. The Au film is later removed by acid boiling in nitric acid. The laser cutting process is completely based on CNC machine language. Therefore arbitrary shapes can be cut out such as lines, squares, etc. with the ultimate goal of isolating a Hall bar around 6 predefined ohmic contacts. We have already designed Hall bar shapes and converted them in CNC language.

Fig 6. Laser Cutter (Alpha) to create holes in the diamond plates (Oxford Lasers).

[5] 3D optical profilometer:

A Bruker 3D optical profilometer (Contour GT-K) with interferometer technology was used to make 3D images of the laser cut holes. This allowed careful monitoring the depth of the hole as a function of applied laser power. In principle much deeper holes can be created but a couple of micrometer suffices for near surface implanted regions. This technique allowed us to calibrate the milling process.
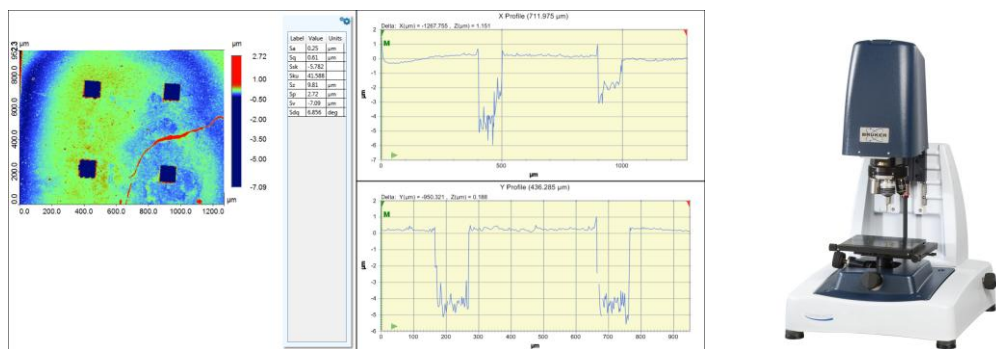

Fig 7. 3D profile (left) obtained of the laser cut holes using the optical profilometer (right).

[6] Semi-automatic wire bonding:

A semi-automatic aluminum wedge bonder (Bondjet BJ715/815 – Hesse & Knipp) was used to make bond wires to the contacts on the diamond plates. This was an extremely reliable process with diamond contacts made of active braze alloy, which consists of gold and bonds easily.

Fig 8. Semi-automatic wedge bonder to make aluminum wire bonds to the braised contacts.

[7] Cryogen-free dilution refrigerator:

For the low-temperature measurements we used a cryogen-free (CF-450) dilution refrigerator from Leiden Cryogenics. This system (Fig. 9) was recently commissioned and reaches a base temperature of ~12 mK and is equipped with high frequency coax lines for RF measurements. The system is equipped with a Cryogenics Inc. 3D vector field magnet with a range of 9-1-1T for Hall measurements and magneto-resistance studies. We can perform arbitrary field rotations up to a field of 1T, which is useful for the determination of anisotropy in samples. It comes furthermore with an insertable probe that allows quick cooldown and characterization of samples down to ~40 mK. Finally, there is an option for placing an optical window in the vacuum cans to shine light onto the sample directly, but this has not been explored yet as it impacts on the base temperature of the fridge.

However, since the system is equipped with a superconducting magnet, we cannot perform Hall measurements while the probe (and magnet) are warmer than 5 K. We can therefore only extract mobility and density measurements for temperatures less or around 5 K and at room temperature with a permanent magnet around the sample holder. Alternatively, we can use NdFeB permanent magnets on our chip carrier, but the field is not very homogeneous. To overcome this issue, we have set up a Hall system with room temperature magnets around a Janis LN_2 flow cryostat.

A new probe for the dilution fridge has been designed by Leiden Cryogenics and will arrive in our lab shortly. It will come with 4 optical fibers (2x VIS and 2x NIR bands) going down in capillaries from RT to a low temperature-collimating lens, which focuses the light. In addition, this probe will have mid-range coax cables and very high frequency coaxes on top of DC wires to electrically characterize our samples when they are cooled down to ~40 mK and subject to large magnetic fields. Our existing probe does not have a very high frequency coax, which prevents us performing low-temperature spin resonance spectroscopy studies. The new probe will allow us to also investigate optoelectronic studies, i.e. photoconductivity studies to probe defect states in the materials used.
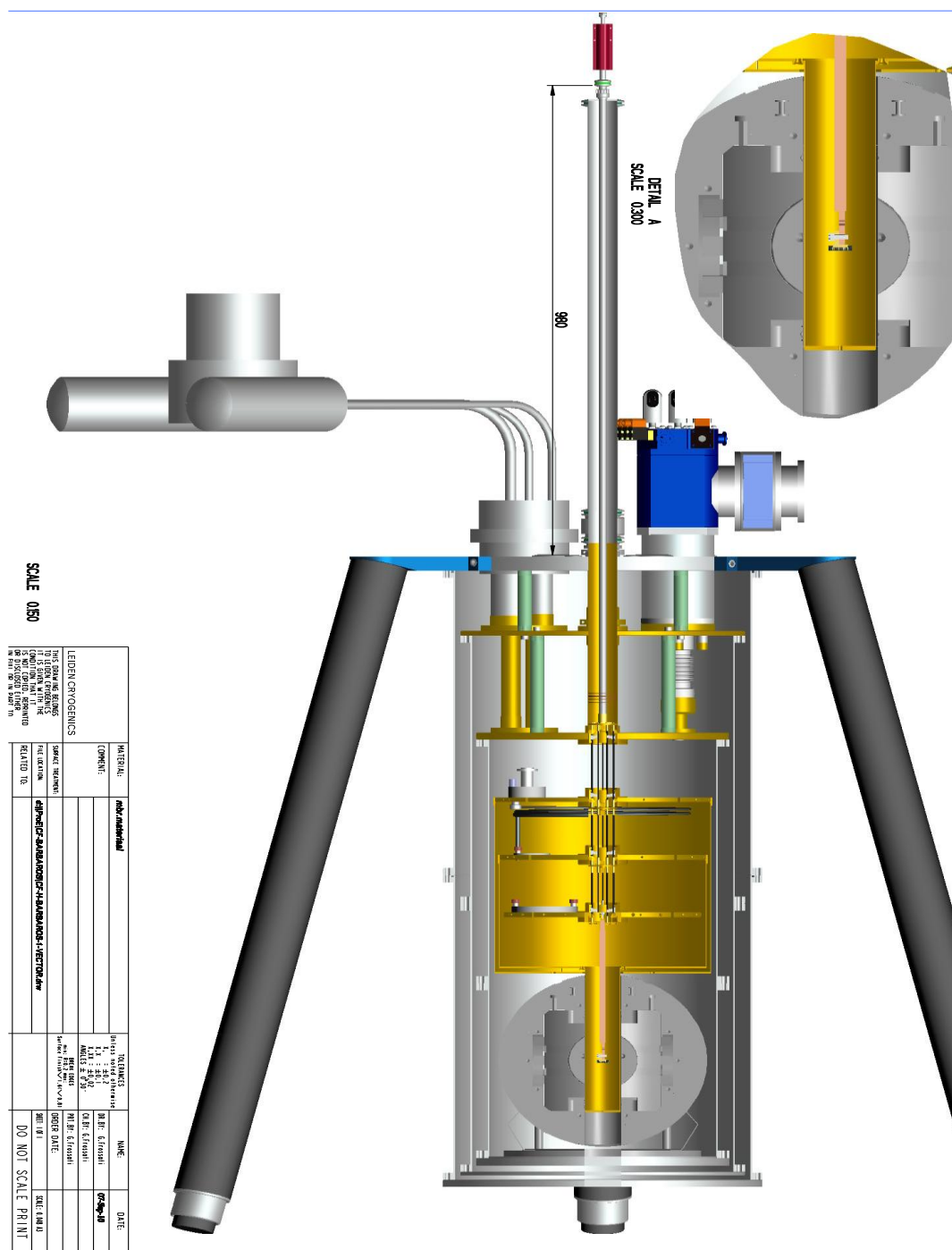
Fig 9. Cryogen-free dilution refrigerator with insertable probe into a 3D vector magnet (90 degrees rotated). The insert cools down to ~12 mK and the probe cools down to ~40 mK. The insert shows the sample in the vector magnet at the end of the insertable probe. The 50 K, 3K, STILL, 50mK and Mixing Chamber (MC) plate are visible from top to bottom, respectively. The probe and plates have heaters to warm up the sample to ~2 K.

The experimental infrastructure required to characterize such buried layers is now available in our laboratory, as evidenced by low-temperature measurements we have performed on type-I and type-II superconducting films of aluminum (Al) and niobium (Nb), as a starting point. The critical temperature and magnetic field(s) of these films can be extracted using the PID-controlled heaters in our dilution refrigerator and the 3D magnetic vector field, respectively. The exact values for T_c and H_{c1} and H_{c2} depend on parameters such as film thickness and purity of the metals used. We have also observed a strong orientation dependence of the superconducting properties of such films with respect to the external magnetic field applied. This is all textbook behavior and illustrates our capability.
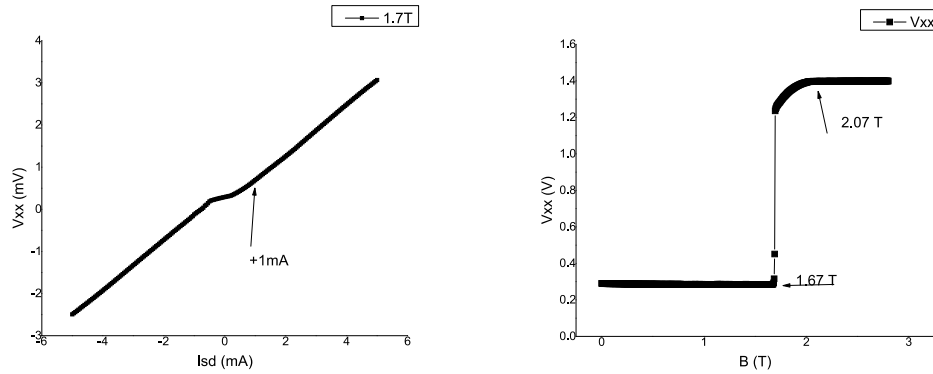
Fig 10. Superconducting properties of a niobium (Nb) film at a fridge temperature of 4-5 K. (Left) Superconducting gap in the I-V for a field of 1.7 T. (Right) magnetic field dependence for ~1 mA through the Nb film. Both T_c as well as H_{c1} and H_{c2} can be extracted from these measurements.

To demonstrate our capability for performing anisotropy measurements with our 3D vector magnet, we have performed rotations on a commercial (GaAs/AlGaAs) cryogenic Hall sensor (Magcam.com). The figure below illustrates the obtained Hall response at constant current while rotating the magnetic field at 0.5 T in the x-y plane (z field=0 T). Note that the Hall sensor is mounted parallel to the z field. The absolute value of the Hall resistance (R_{xy}) shows clear oscillations with maxima for perpendicular field orientation to the sample. The Hall resistance goes to zero when the B-field is parallel to the sample. Here the sample resistance (R_{2T}) is minimal also due to the absence of weak localization.
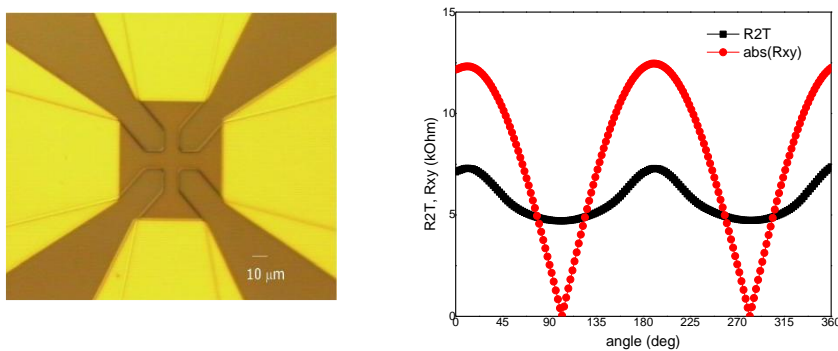

Fig 11. (left) Optical microscope image of the Magcam cryogenic Hall sensor. (right) Angular dependence of the Hall sensor for a 2π field rotation in the x-y plane taken at 4-5 K for 0.5 T and 100 μA.

[8] Janis Hall effect cryostat:

In order to determine carrier mobility, density and sample resistivity at various temperatures, we have set up a flow-cryostat that fits in between the poles of a RT electromagnet. We have used commercial Hall probes and Gauss meters to verify the amplitude of the magnetic field in between the pole pieces and have established a non-linearity between current and B-field at high field range (accounted for in the software by non-linear fitting curve). In addition, we found a ~10 mT offset at zero applied field.

The system is now completely computer programmable and one can perform I-V measurements in a van der Pauw geometry to measure sample resistivity versus temperature. In addition one can measure the Hall voltage either by symmetrization or by sweeping the B-field at constant current. Both methods should reveal the similar values for the carrier density. Indeed the consistency of the two techniques was verified on hydrogen-terminated diamond Hall bar structures and commercial Hall probes and other samples (ITO films).

We have used a Janis flow cryostat (ST-300S) with room temperature operated electro-magnets (Kepco BOP72-28) for the Hall effect analysis, c.f. Fig. 12. The DC magnetic field can be swept over a range of -0.8 to +0.8 T and the temperature can be controlled from RT down to 77 K (or even 2 K for LHe). The resistivity and Hall voltages of the films were extracted using a 4-terminal van der Pauw geometry. Here electric contacts are made to the corners of a square piece of the film to be investigated. We used Keithley instruments: i.e. a 6220 current source, a 2000 voltage meter and a 6487 current-meter to measure the current that flows through the films. A 7001 matrix switch module in combination with a 7065 Hall effect card are essential to cycle through the different current-voltage configurations in order to efficiently extract the correct averaged longitudinal (for resistivity) and Hall voltages. The switch can also be bypassed in case of a 6-terminal Hall bar geometry (adds noise). We have also used a SR560 voltage pre-amplifier for spectral filtering and increasing signal/noise ratio.
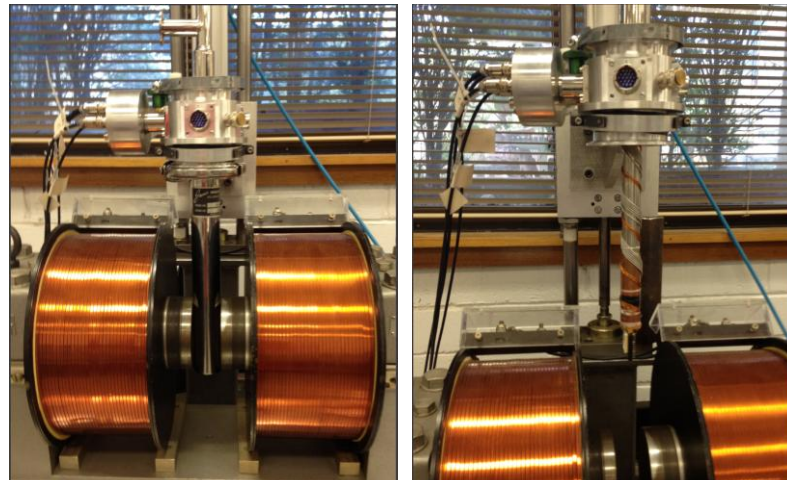

Fig 12. Janis flow cryostat with RT electromagnets for Hall analysis vs. temperature. (Left) Radiation shield and vacuum can in place. (Right). Radiation shield and vacuum can removed to illustrate the Cu cold finger loom wires and 6 tri-axial coax cables to a 24-pin sample carrier (white alumina one). A thermometer and heater are embedded in the finger.

[10] Polishing the alloyed contacts on the diamond surface to smooth for wire bonding

After making the ohmic contacts to the buried layer in diamond by active braze alloying and annealing, we remove the unwanted material (to avoid shorting between electrodes) by polishing back to the diamond surface (c.f. Fig. 13). A flat surface is also required for the wire bonding to the electrodes. The diamond needs to sit as horizontal as possible with respect to the rotation polishing wheel to avoid polishing off the edges and sides of the square diamond plate. If not, the alloyed contacts near the edges of the diamond plate will be polished off. This is the reason we have come up with a new method (laser cut a 2D array of holes closer together) to make multiple contacts on the implanted diamond plates to

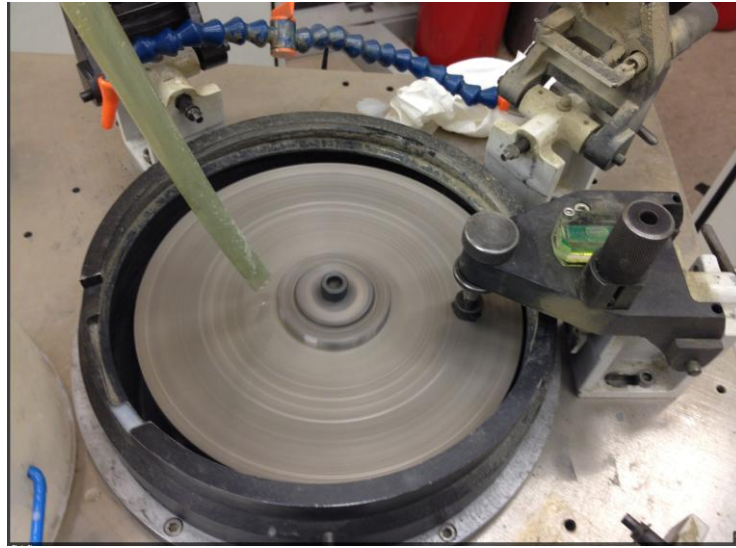maximize measurement 'real estate'.

Fig 13. Polishing wheel lubricated by DI water with our B-implanted diamond sample held in place (upside down) using crystal bond. Care has to be taken to polish the plate uniformly.

Results and Discussion:

In this section we will discuss results of several key experiments [1-6] as proposed in the project description. Preliminary Experimental results of related systems will be presented in the Appendix.

The following key experimental results will be presented here:

[1] Raman analysis of hot-implanted diamond plates beyond the standard graphitization limit

[2] Electrical characterization of B-implanted (hot) diamond beyond the graphitization limit

[3] AFM characterization and Raman analysis of superconducting B-NCD

[4] Electrical characterization of superconducting B-NCD

[5] Raman analysis and electrical characterization of P-doped graphene CVD grown on HOPG

[6] Electrical characterization of the buried graphitic layer (He implanted) using a LN_2 Hall setup

[1] Raman analysis of hot-implanted diamond plates beyond the standard graphitization limit

We have implanted diamond plates at 2 MeV with boron doses well beyond the graphitization limit. Although such fluences ($1x10^{16}$ - $1x10^{17}$ B/cm^2) would normally create buried graphitic layers after high temperature annealing (HTA) when implanted at RT, when the implantation is instead carried out with the sample held at elevated temperatures, the implanted layers do NOT transform into a graphitic layer even after HTA at 1300°C. A Japanese group recently reported similar results in the low fluence/energy regime [7-9] and we have basically verified their described method in the regime of high fluence/energy. This is a game changing technique, as previously we had implanted the diamond plates using the CIRA method (keeping the samples at LN_2 temperatures during implant). Some previous experiments on B-implanted diamond (high fluence at elevated temperatures) did not report any evidence of superconductivity was reported down to 40 mK [10]. However, in that work shallow implantations were used and there seems to be a lot of evidence for the presence of graphite-like components in the B doped volume. However, the work did establish that, as predicted, high temperature implantation can be used to inhibit graphitization, especially for very high ion doses. Hence we have used this method to implant 2 diamond plates at elevated temperatures with $1x10^{17}$ – 400°C and $8x10^{16}$ B/cm^2 – 500°C. In Fig. 14 one can see the color contrast between the 2 fluences. The darker sample (right side) is the $1x10^{17}$ – 400°C sample, before HTA.
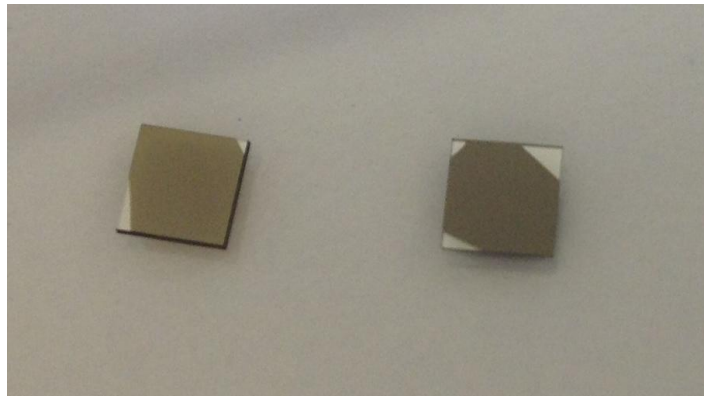

Fig 14. Hot-implanted (in-situ) diamond plates with a boron fluence of $1x10^{17}$ – 400°C (right) and $8x10^{16}$ B/cm^2 – 500°C (left). These samples were acid boiled but not subjected to HTA. The clear areas at the edges of the sample were due to the clips holding the sample in place which shielded the ion beam from impinging on the sample.

The samples were subject to Raman analysis after acid boiling and before HTA.
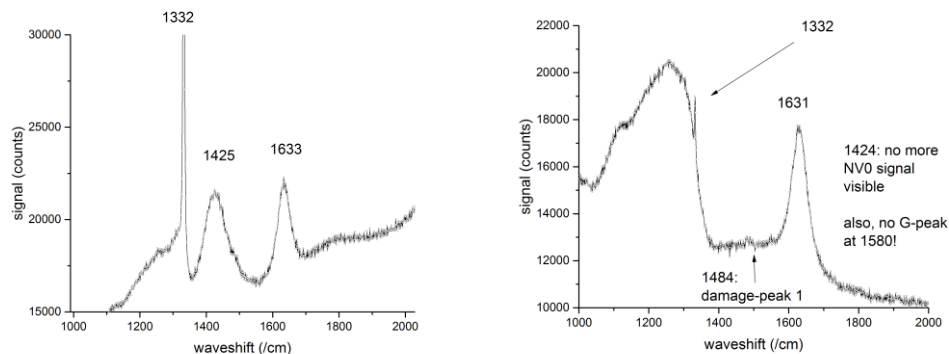

Fig 15. Raman spectroscopy of the hot-implanted samples (left) $8x10^{16}$ – 500°C and (right) $1x10^{17}$ B/cm^2 – 400°C) before HTA where damage peaks are visible from ion-implantation.

After ion-implantation and before HTA we observe damage peaks in the region 1000-2000 /cm waveshift with distinct peaks on the right side of the diamond peak (1332 /cm). Compared to a pristine diamond plate the diamond peak and all other features such as NV^0 and NV^- reduce in intensity. As can be seen in Fig. 15, for both samples there is a damage peak visible at ~1631 /cm. This common damage peak is due to a split-interstitial and anneals out at elevated temperatures, as we will show later. It has been reported previously in the literature and is caused by high-energy implantation in particular.

The 1425 /cm peak visible in the $8x10^{16} - 500°C$ sample could be related to the NV^0 related ZPL, but is not visible in the spectrum of the $1x10^{17}$ $B/cm^2 - 400°C$ sample. Unfortunately, when the HTA was performed at 1500°C for 10-15 minutes these samples collapsed into a graphitic phase throughout the bulk of the crystal. Possibly, a poor vacuum (caused by metal films desorbing from the walls of the e-beam evaporator system, caused rapid degradation of the material. Previously though, we have annealed samples up to 1700°C without too much graphitization occurring.

After this unfortunate HTA outcome, we had our pyrometer serviced (certificate of calibration) to know the exact temperature during the annealing process. This is how we know that in previous runs we annealed at much higher temperatures than previously estimated. The charge state of the battery in the pyrometer is also a variable needs to be carefully monitored, as it can otherwise display the wrong filament current and therefore temperature during the annealing process. The HTA process needs high levels of control to avoid graphitization, while still achieving the goal of effective annealing of defects.
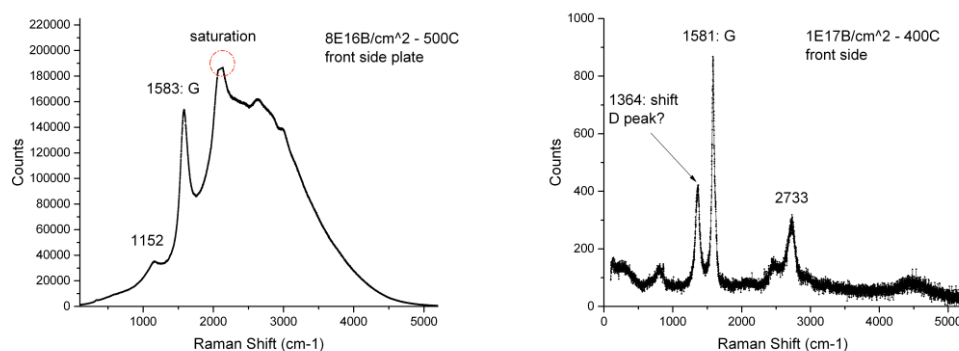

Fig 16. Raman spectroscopy of the graphitized samples (left) $8x10^{16} - 500°C$ and (right) $1x10^{17}$ $B/cm^2 - 400°C$, after HTA at 1500°C for 10-15 min. Note large G-peaks at ~1581 /cm.

As mentioned, after HTA these 2 plates ended up as crumbled pieces of diamond with lots of graphitic material everywhere. It literally looks as the crystal exploded to graphite from the inside out. This could be caused by the swelling of a graphitic sp2 state in a sp3 diamond matrix. The corresponding Raman spectra are shown above in Fig. 16. Large G-peaks (graphite) around 1581-1583 /cm can be observed. In addition, there is no sign of a diamond (D) peak anymore at 1332 /cm. The $8x10^{16} - 500°C$ sample does show a peak around 1152 /cm and the $1x10^{17}$ $B/cm^2 - 400°C$ sample shows a peak at 1364 /cm and another peak at 2733 /cm, which are not accounted for yet. Interestingly, the $8x10^{16} - 500°C$ sample displays still a large photo-luminescence background, in contrast to the $1x10^{17}$ $B/cm^2 - 400°C$ sample. Under the microscope, this diamond plate looks still more or less intact.

After this set back, we decided to stay away from 1500°C (rapid graphitization has been reported for T > 1450°C). Instead we limited the annealing of the samples to 1300°C for 10-15 minutes, although 1450-1500°C might be superior for the incorporation of B in the diamond lattice. These details are to be sorted out in the future. Ideally, a dedicated annealing furnace needs to be setup where outgassing from the walls of the furnace cannot take place. Even more ideal would be to anneal the samples under high pressure, high temperature (HPHT) conditions where diamond is the stable carbon allotrope. (We do not at present have access to such a facility, although we do have a collaborator with contacts in Russia that routinely use such a HPHT process (see section [7] in the Appendix).

We have continued with the hot-implantation technique on 2 more diamond plates. At first, we have

implanted a diamond plate with 2×10^{16} B/cm^2 – 600°C and another plate at 1×10^{17} B/cm^2 – 600°C, followed by acid boil, and HTA. The fluence of these samples should allow the carrier density to reach above the metal-insulator-transition (MIT) at RT. This assumes that we have a high level of activation. We have performed Raman spectroscopy on this new set of plates, before and after HTA, to work out if the annealing time and temperature is sufficient to activate the boron dopants in the crystal and repair some of the broken bonds created by the 2 MeV ion beam. The Raman spectrum for the 2×10^{16} B/cm^2 – 600°C sample is shown in Fig. 17 (before HTA black, unimplanted area in blue).

We have used the *TRansport of Ions in Matter* (TRIM) simulation tool included in the software *Stopping and Range of Ions in Matter* (SRIM) [6] to simulate the end of range (1.38 μm) concentration of boron and the number of vacancies created by the ion-implantation process for an energy of 2 MeV, and a fluence of 1×10^{15}B /cm^2. The boron concentration at this depth is expected to be just over 1×10^{20}/cm^3 with a peak vacancy density of ~1×10^{22}/cm^3 (a factor of 100x higher). Using room temperature implantation, and the need to avoid graphitization, we estimate that at least 40 repeated boron-implants and subsequent high-temperature annealing steps would be required (for a fluence of 1×10^{15}/cm^2) to dope the diamond close to the metal-insulator-transition value of 3.9×10^{21}B/cm^3 (MIT) (the exact value depends on the crystal quality of the diamond (another study showed a MIT value of 4.5×10^{20}/cm^3) [3-4]).

However, using the hot-implantation technique we can implant at much higher fluences i.e. $> 1 \times 10^{17}$B /cm^2 whilst still avoiding graphitization. In this case, the B concentration should reach just over 1×10^{22}/cm^3 if the doping profile is not changed. This should be high enough to exceed the hole carrier metal-insulator-transition even if the activation is not close to unity. However, electrical traps that remain in the diamond after HTA can still reduce the carrier density of holes, especially at low temperatures. Even larger-fluence implants can be achieved by lowering the ion-beam energy from 2 MeV to say 1 MeV, which significantly enhances the beam current and reduces the total implantation time and practicality of the process.

For the Raman spectroscopy it is important to use an objective with a high magnification (50x) in combination with a high numerical aperture (n/a). The high magnification objective allows spectral information to be gathered from a more spatially resolved section of the diamond due to the smaller depth of focus. Since the implanted boron ends up only in a 100 nm thick layer, less than 2 um below the diamond surface. The defect signals observed are mostly from the diamond cap above the layer. To increase the signal to noise ratio of the defect peaks we used averaging of multiple spectra and where necessary increased the power density of the incoming laser light.
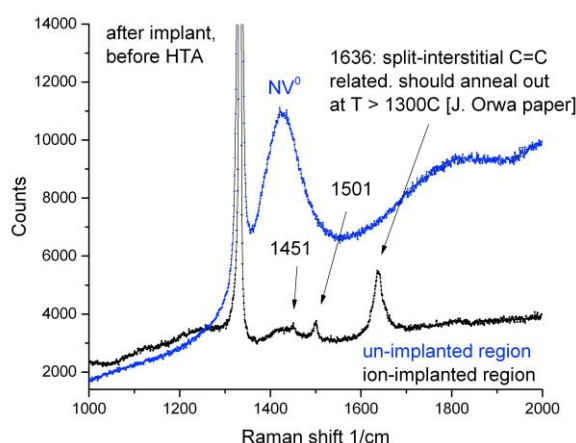

Fig 17. Raman spectrum of the hot-implanted sample (2×10^{16} – 600°C) before HTA (black). For comparison, we also show in the un-implanted section of the diamond (blue).

There are several defect peaks visible in the 1300-1800 /cm range, related to the ion-implantation process. There is a small peak visible near 1451/cm, a larger peak at around 1501/ cm and a large peak

at 1636 /cm. The latter peak has been attributed to a split-interstitial and anneals out above 1300℃ (as will be shown later) [11-13]. Interestingly, the implantation process quenches the NV^0 signal. Sometimes the NV^0 peak is buried in (background) PL signal and can be seen by performing Raman spectroscopy at LN_2 temperatures. As it turns out, the NV^0 peak increases in intensity again after HTA, as we will show later.

Next, we show the $1x10^{17}$ B/cm^2 – 600℃ before HTA and then the ones for $2x10^{16}$ B/cm^2 – 500℃ and $1x10^{17}$ B/cm^2 – 400℃ after HTA, for comparison. If the peaks observed in Fig. 18 are really due to ion-implantation process, they should appear also in samples that are hot-implanted at the same temperature but with a slightly higher fluence.
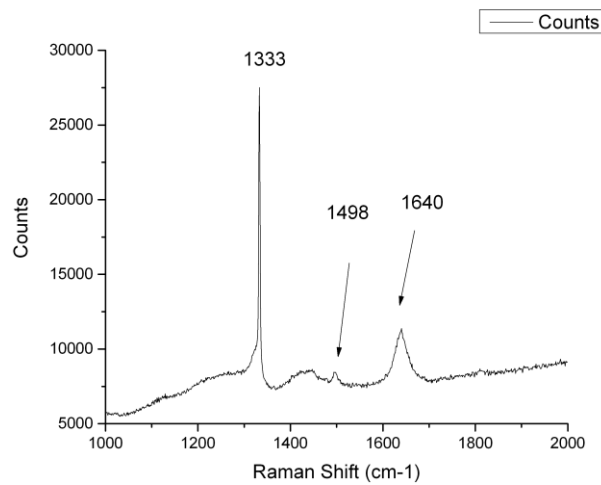
Fig 18. Raman spectrum of the hot-implanted sample ($1x10^{17}$ B/cm^2 – 600℃) before HTA.

In the Raman spectrum we observe again several defect peaks associated with the ion-implantation process. At 1498 /cm we find a small peak and a big peak around 1640 /cm. These peaks were observed for the $2x10^{16}$ B/cm^2 – 600℃ sample too. Next, we show the result of HTA on the spectra.

Finally, note that the diamond peak at 1333 /cm can become very asymmetric in shape, i.e. a dip can develop on the right side of the peak. This dip was previously associated a high carrier density coupled to the C=C vibrational state, i.e. a Fano resonance [20] where the continuum is created by the B-implantation process. We have observed a similar signature (Fano resonance) in B-NCD material from Cardiff University that shows superconductivity at ~2 K. If so, hot implantation without HTA already creates a high number of charge carriers in the diamond (activation by in-situ annealing).

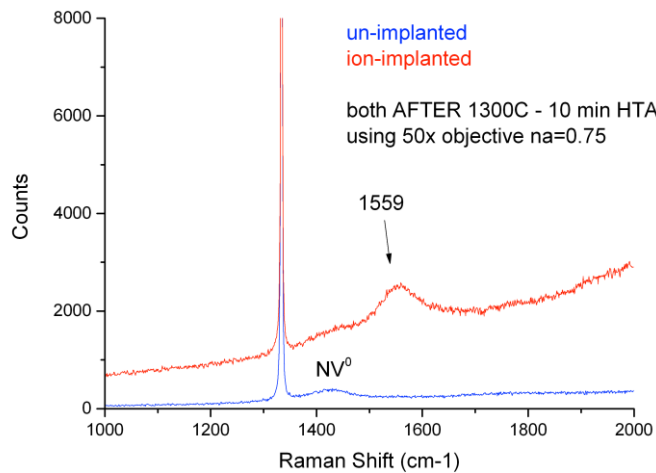*Fig 19. Raman spectrum of the hot-implanted sample (2x10^{16} B/cm^2 – 600°C) after HTA.*

After HTA, there seems to be no more defect peaks visible in the 1000-2000 /cm waveshift range, except for a 1559 /cm peak (Fig. 19). This peak could be a graphite peak, but normally that one sits at higher values, i.e. 1580-1590 /cm. The peak is most likely due to some form of amorphous sp2 bonded carbon. The Raman spectrum for the 1x10^{17} B/cm^2 – 600°C sample after HTA is shown below.
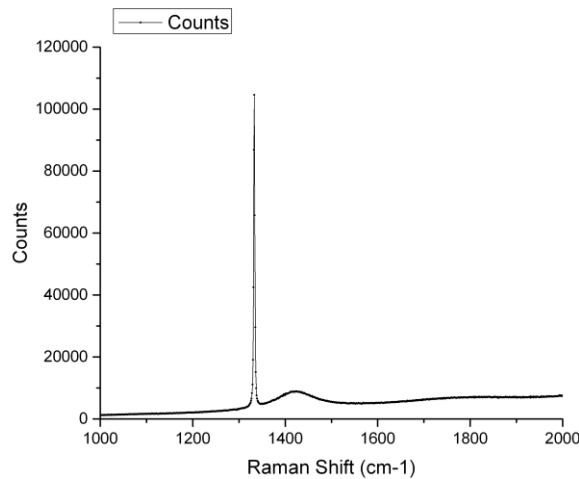
*Fig 20. Raman spectrum of the hot-implanted sample (1x10^{17} B/cm^2 – 600°C) after HTA. The Raman spectrum of the UNIMPLANTED diamond materials can be found in Fig. 19 (blue trace) for the reason of comparison. The spectra look very similar in shape if not identical. **This is a remarkable result for a diamond implanted with such a high fluence.***

It seems that this annealing strategy is good enough to repair most of the (optical) damage associated with the ion-implantation process. In fact, no more damage peaks (as in Fig. 17) can be observed. The diamond peak increases after HTA and the NV^0 peak is visible again. The lattice crystal has therefore recovered as far as this optical spectroscopy is concerned. This does not imply that all the electrical defects have been eliminated. In fact, electrical measurement at low temperatures are necessary to reveal whether residual charge traps in the diamond will result in a reduction in the hole-carrier density in the buried layer. We will show later a large carrier freeze out for the 2x10^{16} B/cm^2 – 600°C sample, but that

the 1×10^{17} B/cm^2 – 600℃ sample remains conducting down to the very lowest temperatures in our dilution refrigerator.

It is important to note that implantations to these very high doses at room temperature followed by HTA always result in the formation of graphitic layers, which display characteristic signatures in the Raman spectrum. The absence of such graphitic peaks in Figs. 19 and 20 is convincing evidence that the hot implantation method allows very high concentrations of B to be introduced into the lattice, while still maintaining the integrity of the diamond lattice structure.

[2] Electrical characterization of B-implanted (hot) diamond beyond the graphitization limit

We have investigated the electrical properties of a B-doped single crystal diamond plate that was implanted at 600°C with 2×10^{16} /cm^2 boron atoms and subsequently annealed for 10-15 min at 1300°C. For this study we have used our cryogen-free dilution refrigerator starting at room temperature and cooling down the sample on our insertable probe. The sample has a 4-terminal device architecture to perform van der Pauw resistivity and Hall measurements (as a function of a DC magnetic field).
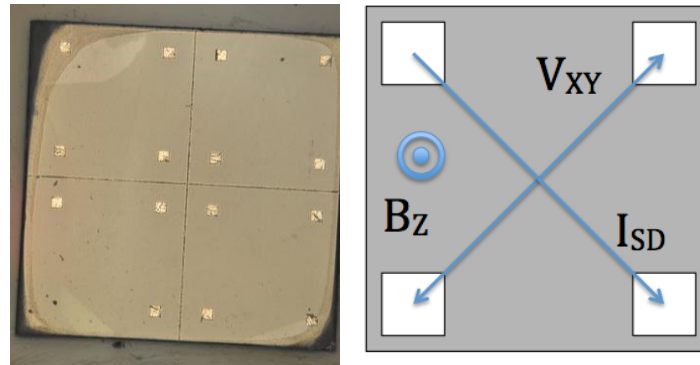
Fig 21. B-implanted diamond plate (left), with 4 contacts in each quadrant to the buried layer. Schematic of the Hall effect measurement setup indicating V_{XY}, I_{SD} and B_Z (right).

Figure 21 shows the diamond plate (left) and the electrical connections made to the buried layer using a gold-based active brazing alloy. The Hall effect measurement schematic is outlined on the right. Typically, a DC current I_{SD} is passed diagonally through the buried layer and the perpendicular Hall voltage (V_{XY}) is recorded as a function of the magnetic field B_Z. We have started our analysis at room temperature taking current-voltage (IV) measurements and extracting the 4-terminal sheet resistance R_s. For the exact thickness of the buried layer we have relied on the doping profile from our SRIM simulations. Roughly, one can assume a layer thickness of ~100 nm thickness to calculate resistivity/3D density.

From Hall measurements at RT (symmetrization of IV traces by rotating the magnet from perpendicular to anti-perpendicular orientation) using a permanent magnet with a magnetic field strength of 0.34 T we were able to extract the carrier density in the buried layer. The result of the Hall measurement is shown in Fig. 22.
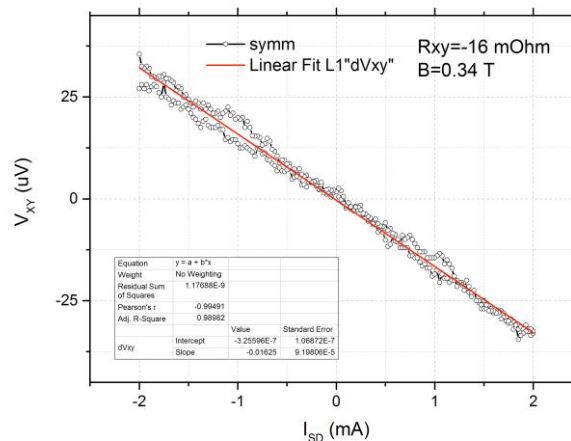

Fig 22. RT Hall measurement by symmetrization of the B-implanted diamond plate.

Here, we ramp the current from -2 to +2 mA and record V_{SD} and V_{xy} simultaneously for both +0.34 T and -0.34 T. The data corresponding to opposite magnetic fields are then subtracted and divided by a factor of 2 to obtain the effective Hall voltage. The resulting slope then represents the Hall resistance over 0.34 T range. The extracted Hall slope in units of Ω/T equals 47 mΩ/T, which corresponds to a 2D carrier density of $n_{2D}=1.3 \times 10^{16}$ /cm^2. Assuming a thickness of 100 nm, and with a sheet resistance of 273 Ω, the 3D density equals $n_{3D}=1.3 \times 10^{21}$ /cm^3 and the resistivity equals $\rho_{xx}=2.7$ mΩ-cm with a mobility of $\mu=1.9$ cm^2/Vs. This carrier density of holes is very close to the SRIM simulated prediction that for this fluence predicts a peak B-concentration of $n_{3D}\sim 2 \times 10^{21}$ /cm^3. This would indicate that we have a reasonably good activation of boron ions using this process (at least 50%).

The temperature dependence of the 2×10^{16} B/cm^2 – 600°C sample is shown in Fig. 23. We have also measured the sample resistance (both 2 and 4-terminal) by taking I-V traces at fixed temperature points. For instance, at RT we find a typical R_{2T} of 800 Ω and a $R_{4T}=220$ Ω. Note that this R_{2T} value obtained here is orders of magnitude lower than what was reported earlier ($\sim$150 MΩ) using graphitized columns (by laser pulsing) as contacts to the buried layer [12]. This indicates that our developed technology really improves on reducing the contact resistance over the older method. At 3-4 K temperatures however, we find that a typical R_{2T} of 5 MΩ and a $R_{4T}=750$ kΩ, i.e. several orders of magnitude larger than at room temperature. This is typical of semiconducting behavior below the MIT.

In Fig. 23 (top) we plot the 2-terminal resistance of the 2×10^{16} B/cm^2 – 600°C sample (van der Pauw geometry as per Fig. 21) as a function of the temperature on (the still plate level of) the probe. We have also plotted the natural logarithm of the conductivity ($1/\rho_{xx}$) vs. 1000/T (bottom) to visualize a thermally activated process at these low temperatures. We extract an activation energy of 1.48 meV for the temperature range between 22 K down to 12 K, before the pre-amplifier went into overload due to the exponentially increasing resistance. The temperature here is that of the mixing chamber.

Note the different temperatures used for the x-axis (T_{STILL} vs. T_{MC}) in Figs. 23 and 24, respectively. These temperatures reflect the sample temperature most closely, as the thermometers on the probe have different optimal operating ranges. For a given temperature, some thermometers can be (partly) in saturation whilst others are operating optimally in their respective temperature range.

In Fig. 24 (top) we plot R_{2T} vs. the temperature (the mixing chamber plate level of) the probe and in (bottom) R_{4T} vs. the temperature (the mixing chamber plate level of) the probe. Basically, the material shows a dramatic resistance increase below 10 K. This indicates that the carrier density is below the metal-insulator-transition (MIT). Upon cool down, charge carriers localize in trap states, resulting in a freeze out that increases the resistance exponentially. The upshot of this is that the 2×10^{16} B/cm^2 sample becomes so resistive that it is not 'measureable' by DC techniques below $\sim$2 K easily. At 3-4 K we have tried to perform magnetic field sweeps to extract the carrier density and mobility. However, the temperature dependence of the sample is so large that any (random) small change in the probe temperature (e.g. sweeping the B-field) dominates the sample resistance, rather than the effect of the magnetic field. Therefore, we have abandoned low-temperature Hall measurements on this sample.

Recently however, we realized that we can get around this issue by fixing the magnetic field for both polarities and perform a symmetrization of the Hall voltage I-V curves. This way, the sample temperature will not change as no magnetic field is swept. But for this sample we cannot operate the superconducting magnet above 4-5 K, which is required to measure the carrier density before it completely freezes out. We expect this to work at LN$_2$ temperatures in our Hall system since the magnet sweeps do not affect the sample temperature directly. However, at present we do not know what the carrier density is of this sample at the lowest temperatures.
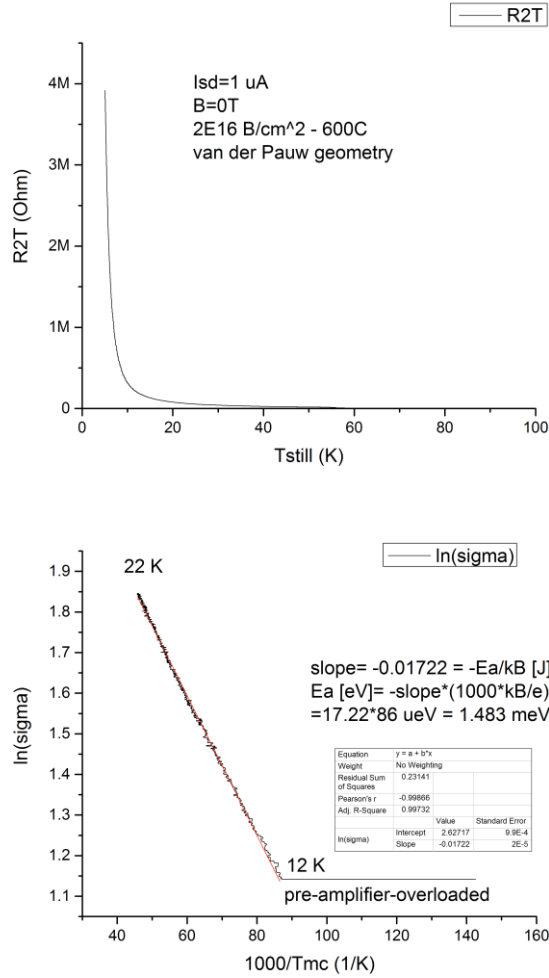
Fig 23. Temperature dependence of the $2x10^{16}$ B/cm² – 600°C implanted diamond plate. The 2-terminal resistance showing a dramatic increase below 10 K (top). We plot ln(σ) vs. 1000/T (mixing chamber) to see if the data follows an activation behavior (bottom). A very linear dependence is observed between ln(σ) and 1000/T, with an extracted Ea of 1.48 meV.

The 4-terminal resistance R_{4T} can be used to calculate and plot the conductivity as a function of the inverse temperature to try and extract the activation energy. In this case, between 22 K and 12 K there seems to be a very exponential decrease of the conductivity with decreasing temperature (freeze out). Since the dependence of Fig. 23 (bottom) is linear on a logarithmic y-axis, we can use the slope as an estimate for the activation energy. For an activated process in a semiconducting material the electrical conductivity changes as $\sigma(T) = \sigma_0 \exp(-E_a/k_B T)$, where Ea is the activation energy (eV), T is the temperature in units of K, and k_B is the Boltzmann constant. Taking the natural logarithm and rearranging we find that Ea (eV) = ln(σ)/(1000/T) (1000 k_B/e).

The first term is basically the slope of Fig. 23 (bottom), wherefore the energy gap can be given by the following relationship after finding the slope: Ea (eV) = slope (0.086). Unfortunately, we have only collected conductivity data for this small range as the pre-amplifier went into overload due to the resistance increase and the limited operating range of the mixing chamber thermometer. Fortunately, this is the temperature range where the resistance changes most dramatically, c.f. R_{2T} in Fig. 23 (top), and we can assume that the fit can be used for parameter extraction. If this energy gap is real that it can be used as a measure how far we are away from the metal-insulator-transition point, where this energy gap should become zero (metallic).

Furthermore, note that this fit to the data rules out a variable-range hopping (VRH) model, since that would correspond to the conductivity depending on temperature in the following way: $\sigma(T) = \sigma_0 \exp(-[T_0/T]^{0.25})$. Therefore, we can rule out a transport where tunneling occurs between two conducting boron clusters [23].
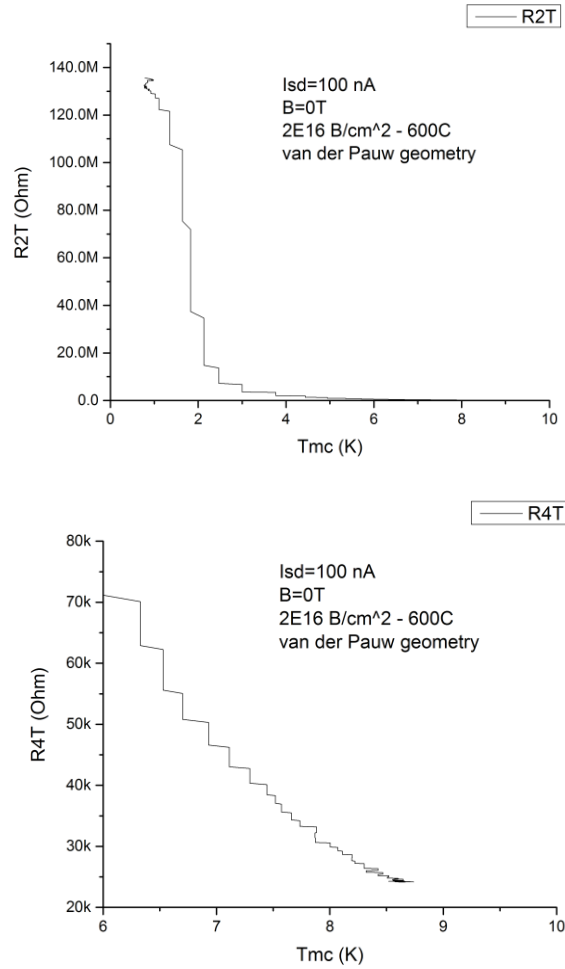

Fig 24. Temperature dependence of the $2x10^{16}$ B/cm^2 – 600°C implanted diamond plate (top) 2-terminal resistance below 10 K showing rapid freeze-out. (Bottom) 4-terminal resistance below 10 K demonstrating the same phenomenon is intrinsic to the material and not contact resistance related. The material is not 'measureable' by DC techniques below ~2 K.

We will next discuss the electrical characterization of a $1x10^{17}$ B/cm^2 – 600°C hot implanted sample. The electrical contacts of this sample are shown in the Fig. 25 below. For our electrical measurements we have focused on the 2x2 contacts in the centre of the plate. The pitch between contacts is 500 μm.
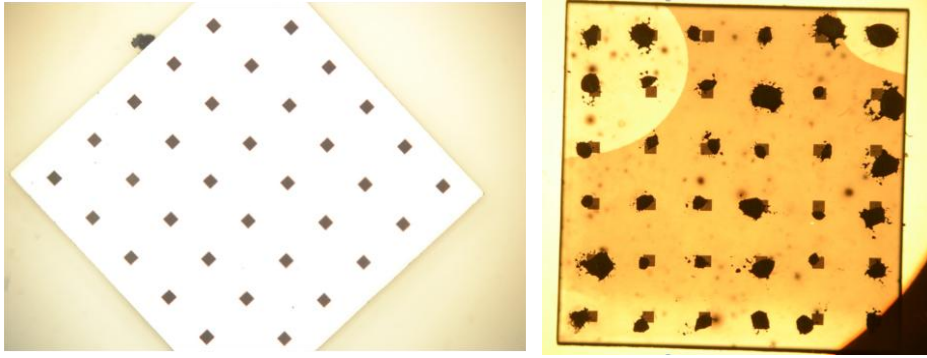
Fig 25. (Left) Back light image of the 1x10^{17} B/cm^2 – 600°C hot-implanted diamond plate with 6x6 contacts laser cut into to the buried layer. (Right) Back light image of the alloyed contacts in the laser cut holes. Note that not all contacts connect to a conducting region due to shadowing from Ag paste.

We will now discuss its electrical properties and compare them to the data for the 2x10^{16} B/cm^2 – 600°C sample. This will be important to estimate what implantation fluence is necessary to reach the metal-insulator-transition critical density in these plates.
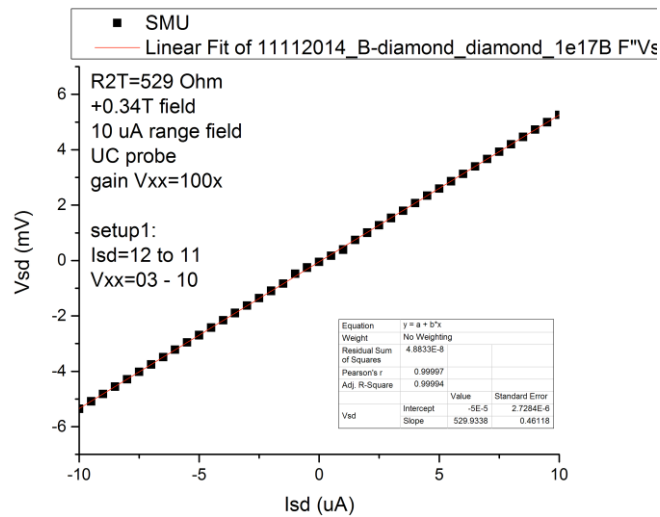

Fig 26. RT I-V of the 1x10^{17} B/cm^2 – 600°C sample. The R$_{2T}$ value equals 529 Ω.

The 2-terminal resistance between two 500 µm spaced contacts is R$_{2T}$=529 Ω, c.f. Fig. 26. The 4-terminal resistance R$_{4T}$=47 Ω, c.f. Fig. 27. For the other (90 degrees rotated) van der Pauw configuration we find that R$_{4T}$=105 Ω. There is therefore a slight non-uniformity in the sample (factor 5x). Note that these values are much lower than for the 2x10^{16} B/cm^2 – 600°C sample, which seems to indicate that we have indeed implanted at a higher fluence and therefore we hope to see that the carrier concentration of the buried layer is also higher as a consequence. The R$_{4T}$=47 Ω, corresponds to a RT resistivity of ρ_{xx} = t$_S$ R$_{4T}$ = 0.47 mΩ-cm and µ=1/(e ρ_{xx} n$_{3D}$) = 8.3 cm^2/Vs, respectively, assuming a sheet thickness of t$_S$ = 100 nm and a carrier density of n$_{3D}$=1.6 x10^{21}/cm^3 c.f. Fig. 29 (lowest density).

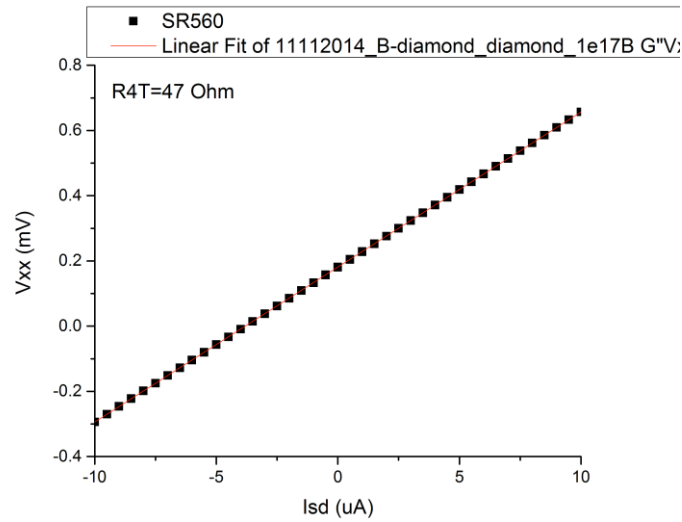*Fig 27. RT I-V of the $1x10^{17}$ B/cm² – 600°C sample. The R_{4T} value equals 47 Ω.*

We have then measured the Hall response at RT by symmetrization. Since this material has a higher carrier density it is harder to extract the Hall slope by symmetrization, as they are inversely proportional to each other. The higher the density is, the lower the resulting Hall voltage. However, we did manage to get an estimate of the carrier density but only by ramping the DC current over a 10 mA range. The resulting Hall data is shown below in Fig. 28.
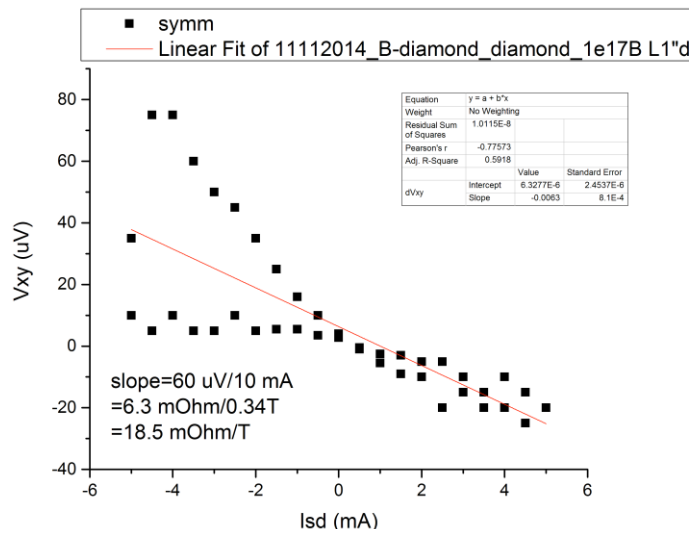

Fig 28. RT Hall data extracted by symmetrization of the $1x10^{17}$ B/cm² – 600°C sample.

The extracted carrier density for this material is $n_{2D}=1.6 – 3.2x10^{16}$/cm². This corresponds to a 3D carrier density of $n_{3D}=1.6 – 3.2x10^{21}$/cm³ assuming a 100 nm thick buried layer. This carrier density is not too different from the $2x10^{16}$ B/cm² – 600°C sample, but the data is too noisy to really conclude with certainty that both samples have different densities from Hall measurements alone. We then cooled down this sample on the probe of our dilution fridge and mapped out R_{2T} and R_{4T} as a function of the temperature. The result is shown below in Figs. 29 and 30.
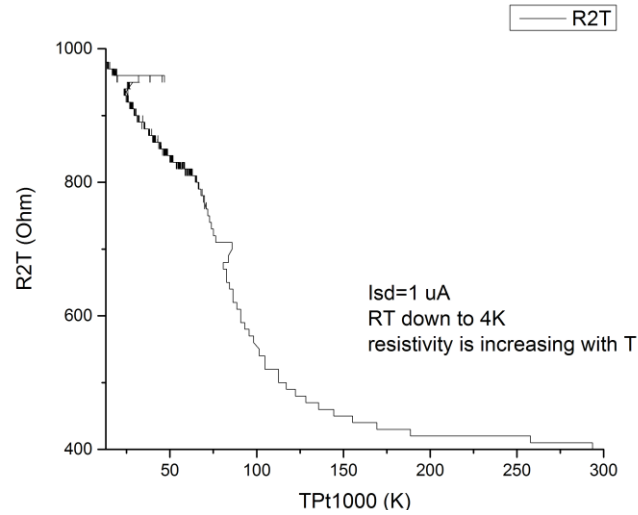
Fig 29. R_{2T} data vs. temperature of the $1x10^{17}$ B/cm^2 – 600°C sample using a 1 μA current.

The 2-terminal resistance basically doubles from RT down to 4 K.
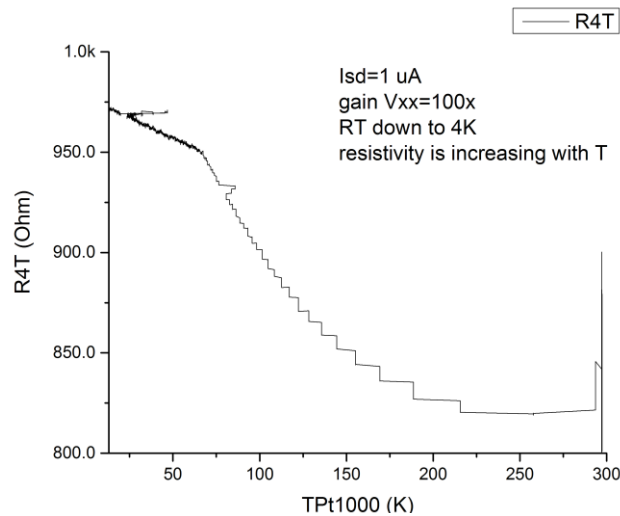
Fig 30. R_{4T} data vs. temperature of the $1x10^{17}$ B/cm^2 – 600°C sample using a 1 μA current.

The 4-terminal resistance of the sample only slightly increases from RT down to 4 K. This is a good sign that we are approaching the metal-insulator-transition (MIT) point, as the 2-terminal sample resistance is not climbing up to MΩ values. Furthermore, at 4 K, the value for R_{4T} stays below 1 kΩ. However, temperature changes caused by sweeping the magnetic field make it impossible possible to extract values for carrier density and mobility at this temperature.

Therefore, we opt for the symmetrization technique, explained above, to find these values. We set our superconducting magnet to a fixed field of +/- 1T and ramp a DC current through the sample from – to + 0.5 mA. The extracted Hall slope corresponds to a value of 0.991 Ω/T, which corresponds to a n_{2D}=6.3x10^{14} /cm^2. Assuming 100 nm thickness for the buried layer we find n_{3D}=6.3x10^{19} /cm^3 for the carrier density at 4 K. The associated resistivity and mobility at 4 K are ρ_{xx}=1.71 mΩ-cm and μ=57.9 cm^2/Vs, respectively.

Now we are going to compare our results to previous attempts to create B-doped layers in diamond.

Note that this ρ_{xx} value at 3-4 K is orders of magnitude lower than that reported at RT in [19], which agrees with the fact that our hole carrier density is much higher. The carrier mobility in [19] increases slightly with lowering the temperature. This could either be due to quenching of the phonon scattering at lower temperatures, and/or because the carrier density is dropping rapidly as a function of reducing the temperature. Here we demonstrate that the carrier density of our $1x10^{17}$ B/cm^2 – 600°C sample at 3-4 K is still larger than that reported in [19] at RT.

The I-V curves underlying the resistivity and Hall data are all linear which demonstrates that the ohmic contacts formed by the active braze alloy have no significant Schottky contacts. This agrees with previous measurement down to the mK regime. This is very important for the correct measurement methodology when trying to observe superconducting transitions in condensed matter.
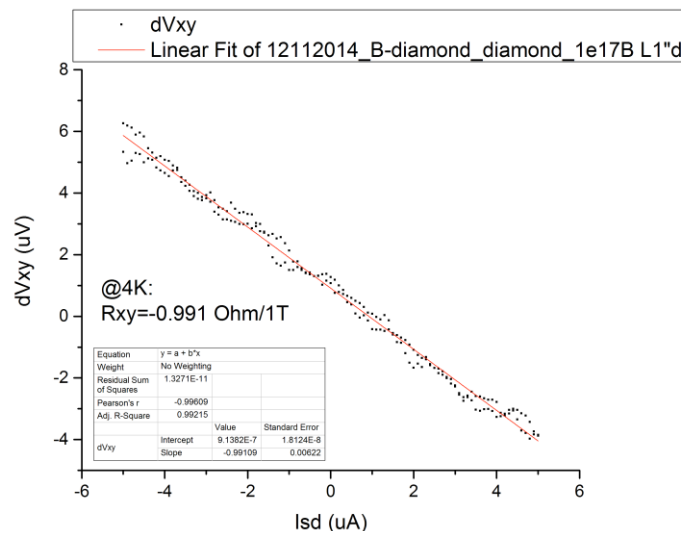

Fig 31. Hall data extracted by symmetrization at 3-4 K using a 1T magnetic field for the ($1x10^{17}$ B/cm^2 – 600°C) sample.

Comparing the carrier density at RT vs. 3-4 K it appears as the cooldown reduces the density from $n_{3D}=1.6 – 3.2x10^{21}$/cm^3 to $n_{3D}=6x10^{19}$/cm^3, which is nearly 2 orders of magnitude difference. Thus, it appears likely that we are close to, but have not quite reached the metal-insulator concentration. We may also have to anneal the diamond plates at higher temperatures (1500°C instead of 1300°C) to improve the activation of B in the diamond crystal or remove electrically active traps in the cap layer that were created by ion-implantation. The Raman spectroscopy analysis did not display significant optical defects in the implanted samples, but that is not to say there are no electrically active trap centers present near the buried layer, which can trap holes during cooldown.

We then cooled the $1x10^{17}$ B/cm^2 – 600°C sample down from 3-4 K to base temperature while recording the sample resistances to look out for a superconducting phase transition.
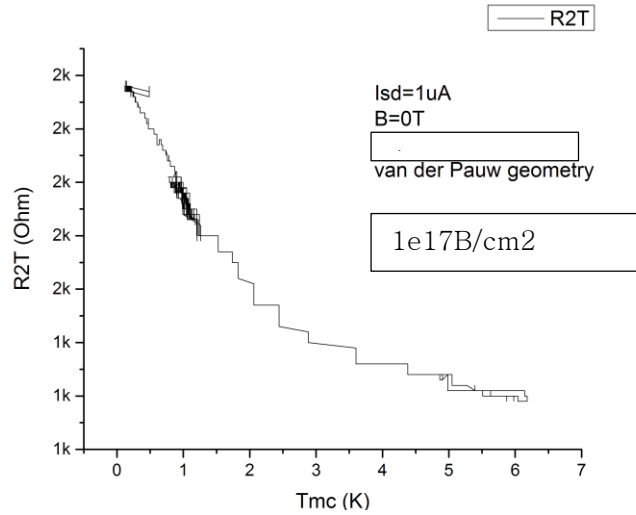
Fig 32. R_{2T} vs. temperature from 3-4 K to base using a 1 μA current ($1x10^{17}$ B/cm^2 – 600°C).
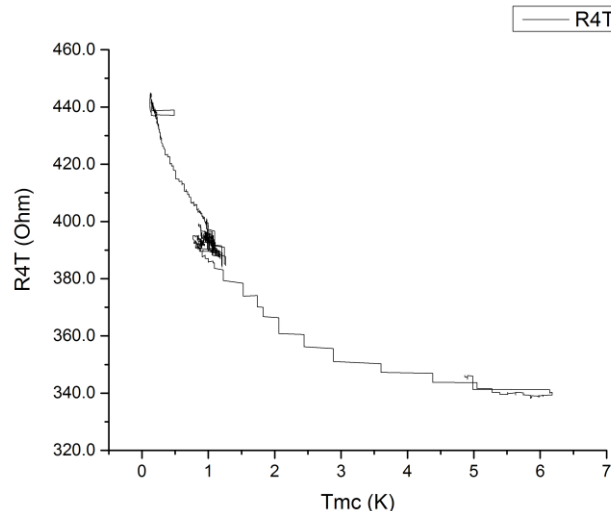
Fig 33. R_{4T} vs. temperature from 3-4 K to base using a 1 μA current ($1x10^{17}$ B/cm^2 – 600°C).

The bad news is that no superconducting transition is visible down to 120 mK (base). The good news is that the sample resistance does not rapidly increase to values exceeding many kΩ. This is in sharp contrast to the $2x10^{16}$ B/cm^2 – 600°C sample. This implies we are very close to the MIT value. We then took an I-V trace at 120 mK to demonstrate that the I-V trace remains linear and doesn't show a sign of a superconducting gap for small DC current values. The result is shown below in Figs. 34 and 35.
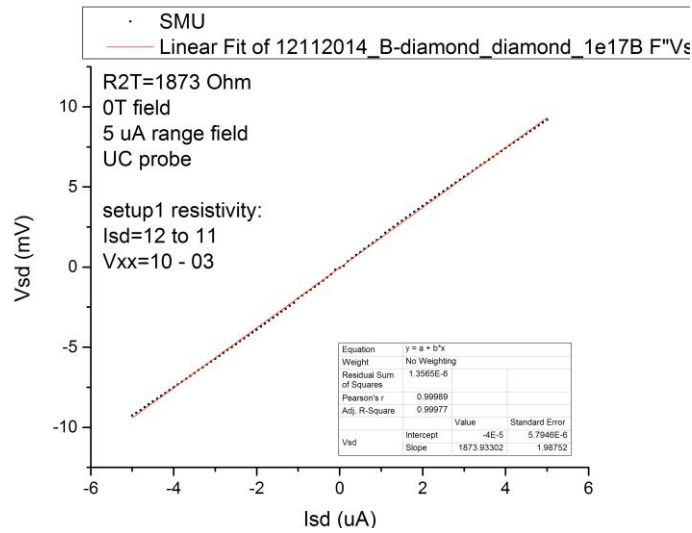
Fig 34. I-V trace at 120 mK at 0T magnetic field. The R_{2T} value extracted is 1.87 kΩ.
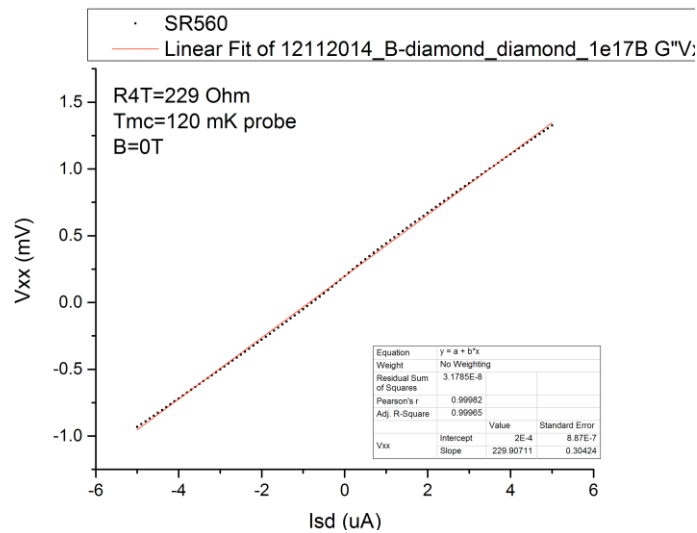
Fig 35. I-V trace at 120 mK at 0T magnetic field. The R_{4T} value extracted is 229 Ω.

The I-V traces are linear but the V_{xx} vs. I_{SD} curve does not display a superconducting gap at low bias at this temperature [13]. It is good to know that the R_{4T} value at this temperature is only 229 Ω, which is promising for future experiments with even higher doping. It furthermore shows that the contact resistance dominates the total resistance by about a factor of 10x and not the intrinsic resistance of the buried layer. The corresponding resistivity at 120 mK equals ~2.29 mΩ-cm assuming a 100 nm sheet.

To summarize our work on the B-implanted diamond samples:

	RT ρ_{xx} [Ω-cm]	RT n_{3D} [#/cm^3]	RT μ [cm^2/Vs]	4K ρ_{xx} [Ω-cm]	4K n_{3D} [#/cm^3]	4K μ [cm^2/Vs]	120 mK ρ_{xx} [Ω-cm]
2×10^{16} B/cm^2 – 600°C	2.7 x 10^{-3}	1.3x10^{21}	1.9	-	-	-	-
1×10^{17} B/cm^2 – 600°C	0.47 x 10^{-3}	1.6 – 3.2x10^{21}	8.3	1.71 x 10^{-3}	6.3x10^{19}	57.9	2.29 x 10^{-3}

Fig 36. Table showing all extracted parameters of the B-implanted samples.

[3] AFM characterization and Raman analysis of superconducting B-NCD

We have continued to analyze the B-doped nanocrystalline diamond film, that shows superconductivity around ~2 K, that we received from Cardiff University (UK). We have used several methods (SEM, Hall measurements, ellipsometry, AFM, Raman spectroscopy and also SIMS) to analyze this CVD grown film. Initial Hall measurements were performed on this material, but since the exact thickness of the B-NCD film grown on top of a silicon substrate was not known, we could not extract a resistivity value and therefore not a carrier density nor mobility. SIMS is the most promising technique for extracting the thickness of the B-NCD film (currently in progress).

Unfortunately, it turns out that the piece of B-NCD we received and measured in our fridge was deposited on a highly conductive silicon substrate. This made the Hall analysis very difficult to interpret as we had a sample with a parallel conduction channel. Furthermore, since this diamond material is black and polycrystalline in nature, it is not very suited for ellipsometry to extract the thickness of the NCD layer on silicon. Atomic force microscopy (AFM) was performed at the University of Melbourne to get a handle on the grain size of the B-NCD and its morphology.
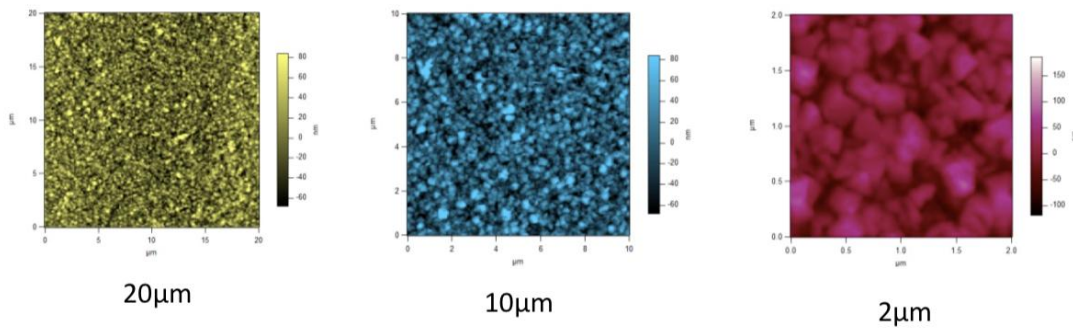

20μm   10μm   2μm

Fig 37. AFM data of B-NCD film taken in 20 / 10 and 2 μm areas. Courtesy of M.R. Notivoli.

The AFM pictures above illustrate the polycrystalline features of the B-NCD from 20 μm down to ~2 μm. Then, in order to establish an estimate of the average grain size a final zoom in was performed on a 300 by 300 nm area, with a typical grain size of at least 150-200 nm. Therefore this material is not ULTRA-nanocrystalline by definition. For comparison, we have grown N-doped UNCD with typical grain sizes of ~5-10 nm. The high-res plot and a 3D plot of a 2 μm-size area are shown below.
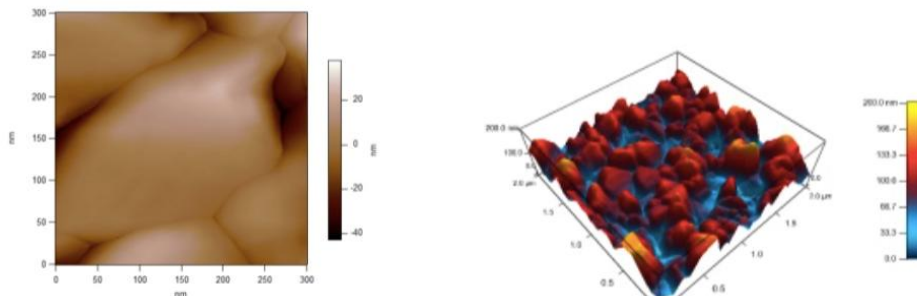
Fig 38. AFM data of B-NCD film taken over a 300 by 300 nm area (left). 3D plot of the AFM data taken over a 2 by 2 μm area (right). Courtesy of M.R. Notivoli.

The surface roughness of the B-NCD material can be extracted from the 3D plot. Looking at the red color on the color bar, we extract an estimated surface roughness of 100 nm. Therefore, to some degree, the surface roughness is indeed determined by the averaged minimum grain size of the material. This extracted roughness value provides a lower bound on the film thickness at least.

We have also performed Raman spectroscopy of the B-NCD film at RT. The resulting spectrum is shown in the figure below.
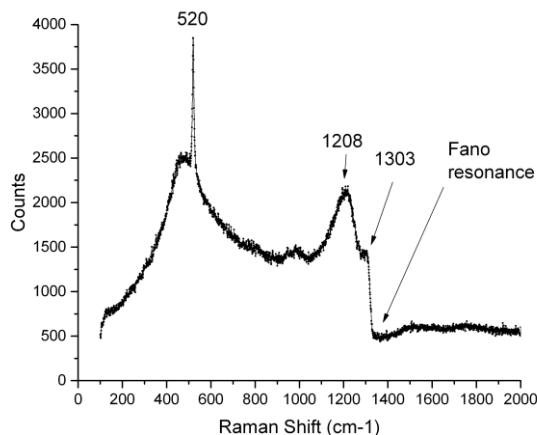

Fig 39. Raman spectrum of the B-NCD film at RT. Silicon peak at 520 /cm is visible.

The silicon (Si) peak at 520 /cm is visible which indicates that the B-NCD film is not very thick; say at least less than 1-2 μm (upper bound of sample thickness). In addition we observe that the diamond peak (D) is quenched (1332 /cm) and a broad peak at 1208 /cm and a shoulder at 1303 /cm is visible. Furthermore, there appears to be a dip directly on the right side of the location of the D-peak, which could be attributed to a Fano resonance, c.f. Fig. 5 in Ref. [21]. According to [21], the Fano resonance is observable as a broad peak at about 1230 /cm and as a deformation of the zone-centre phonon line at 1332 /cm. The depth of this Fano resonance could provide an estimate of the carrier density.

The main difference when comparing this CVD grown B-NCD Raman spectrum with our B-implanted diamond plates is the absence of a Fano resonance (and Si peak obviously) but the presence of a strong D-peak. Furthermore, since our diamond plates contain a lot of nitrogen, we see the NV^0 and NV^- PL peaks. It is not clear at this point, if we will ever observe a Fano resonance in our implanted diamond even once the MIT is reached.

[4] Electrical characterization of superconducting B-NCD

We performed low-temperature electrical measurements on the B-NCD material in the van der Pauw geometry to establish the superconducting phase transition around ~2 K. The sample has a conducting substrate of silicon, which is highly doped (above MIT). Hence, the normal state resistance of the B-NCD film is a parallel combination of electrical current flowing through the B-NCD top film and a current flowing through the Si substrate.
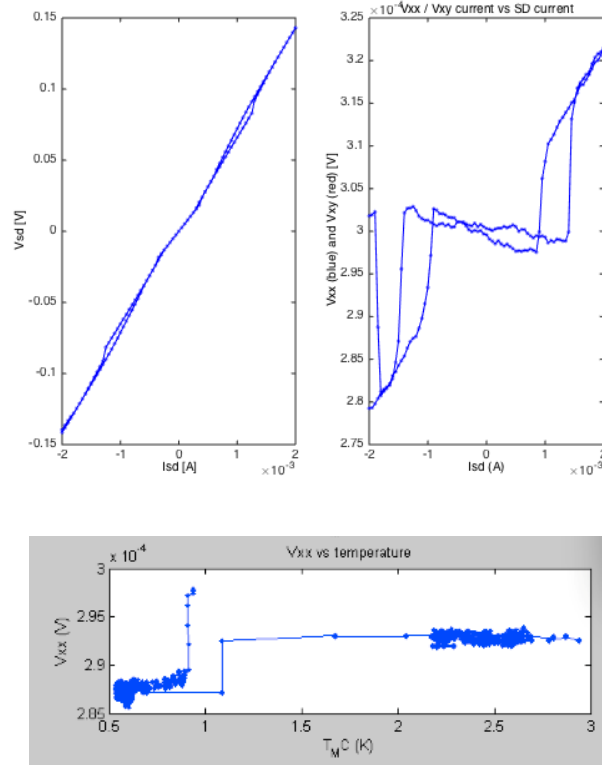

Fig 40. (top) I-V trace (left): V_{SD} vs. I_{SD} and (right) V_{xx} vs. I_{SD} at 100 mK temperature and 0 T magnetic field displaying the superconducting gap of the B-NCD film. The critical current for this material under these conditions is about 2 mA, but very hysteretic. This can be caused by either Joule heating or (de)trapping of vortices in the superconductor.(bottom) V_{xx} vs. T_{MC} trace showing a SC state transition around ~1-2 K obtained during a cool down.

Figure 40 (top) above displays the I-V taken at 100 mK temperature to show the superconducting gap of the B-NCD material. The 2-terminal resistance R_{2T}=71 Ω and the normal state 4-terminal resistance R_{4T}=172 $\mu\Omega$. The voltage pre-amplifier adds an offset to the detected voltage. Note that the up and down trace are not exactly on top of each other (hysteresis). This can be caused by flux trapping or detrapping during the I-V sweep. Since the material is very conducting in the normal state, considerable DC currents (mA range) are required to pick up a longitudinal voltage drop change. But since the total resistance includes the series resistance of the cables, a lot of heating can occur and affect the V_{xx} vs. I_{SD} trace. Ideally, we have this material connected up to low-ohmic coax cables to minimize this effect.

We have also taken temperature dependent data at constant current to work out what the critical temperature for this material is at zero applied magnetic field, c.f. Fig. 40 (bottom). It can be seen that there is a very sudden jump in V_{xx} during cooldown to an offset determined by our voltage pre-amplifier. This is the SC state transition and it happens around ~1-2 K. More data points are required in this regime to map out its precise transitioning from normal to superconducting state.

[5] Raman analysis and electrical characterization of P-doped graphene CVD grown on HOPG

We have performed complementary measurements on phosphorus-doped graphene samples grown in Prof. Grover Larkins group at Florida University as suggested by AOARD. These samples are thought to display magnetic / superconducting phase transitions in the LN$_2$ to RT temperature range. A DC SQUID analysis has shown magnetization changes upon cooling down such samples with different trends whether or not a magnetic field was applied during cooldown. These samples are potentially interesting as they hint at magnetic phases in carbon-based materials, quite similar to what we expect to observe in highly conductive layers in diamond as a result of B-implantation.

We have therefore investigated the electrical properties of phosphorus-doped graphene layers, grown in a CVD reactor using phosphine gas, on pure highly oriented pyrolytic graphite (HOPG) substrates. For this study we have used a conventional Hall system with room temperature electromagnets and a 4-terminal device architecture to perform van der Pauw resistivity and Hall measurements.
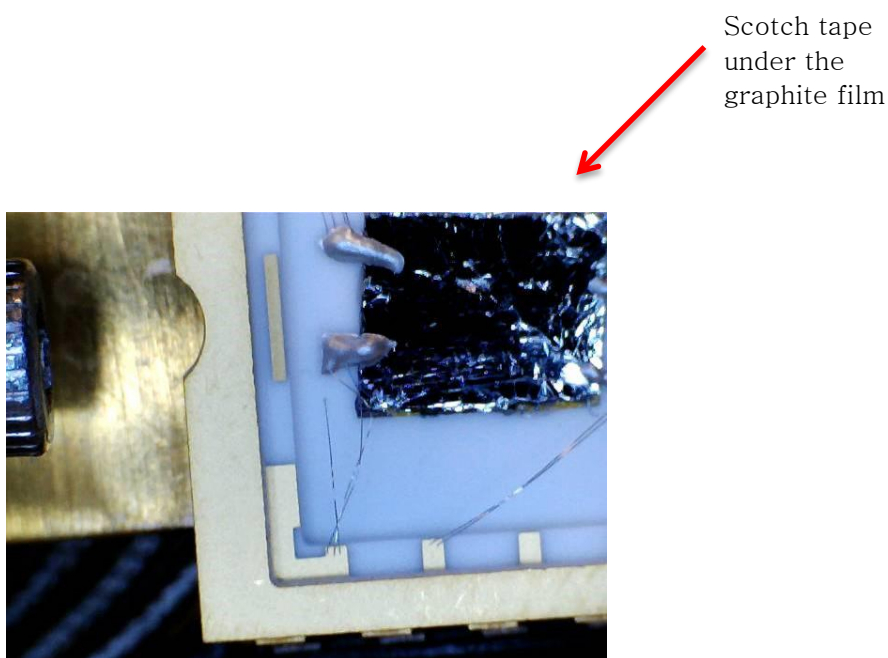
Scotch tape under the graphite film

Fig 41. Image of the Hall system chip carrier, containing 4 contacts to the phosphorus (P) doped graphene layers on highly oriented pyrolytic graphite (HOPG) substrate. After growth, the material is peeled of from a bulk graphite substrate using the Scotch sticky tape (yellow) transfer method. Wire bonds to the white alumina chip carrier back plane are made first, after which contact to the material is made by 2-component silver epoxy, which solidifies.

Figure 41 shows the film and the electrical connections made to it using 2-component silver epoxy. To harden the epoxy we anneal the samples for 20 minutes on a hotplate at 150C. We have started our analysis at room temperature taking current-voltage (IV) measurements and extracting the 4-terminal sheet resistance. Since the exact thickness of the material is not known and the graphite substrate also conducts (parallel conduction channel), it is not straightforward to extract parameters such as resistivity, mobility, etc. Finally, we don't know for sure if this material behaves as a (quasi) 2D conductor or not.

In order to establish how many graphene layers are grown on top of the HOPG we have performed Raman spectroscopy at low temperatures (85 K) to narrow the spectral features. From the intensity ratio of the 2D and G peaks an estimate of the number of graphene layers can be made. Figure 2 shows the Raman spectrum obtained. Several features stand out. One can observe the D peak at 1346 /cm, the G peak at 1584 /cm related to graphite as well as a peak at 2453 /cm and a 2D band around 2719 /cm. We

observe a G/2D peak ratio of about 2x, which indicates a multilayered graphene layer of 5-10 layers. Since each graphene layer is 0.2 nm thick, the total graphene film could be ~ 2 nm thick on top of a thick graphite film of HOPG.
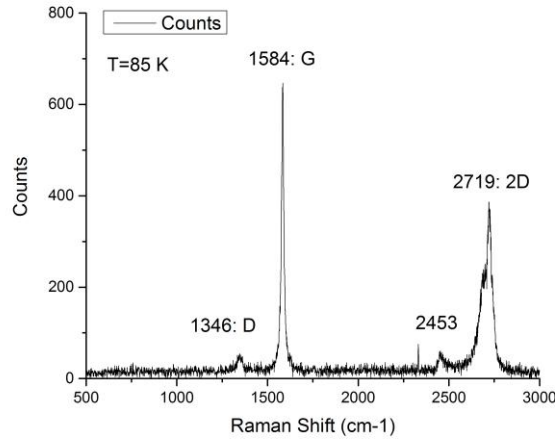

Fig 42. Raman spectrum (532 nm laser) of a P-doped graphene film on HOPG at 85 K, taken with a high N/A 50x objective. The spectrum has 2 distinct features: a sharp G peak at 1584 /cm and a broad 2D band at around 2719 /cm.

The current-voltage (IV) measurement is shown in Fig. 43. Here we ramp the current through the film between the contacts on one side of the van der Pauw square and measure the local voltage drop on the opposing side. The measurement is taken at room temperature in zero magnetic fields. It can be seen that the 4-terminal resistance extracted from the linear IV corresponds to 45 mΩ, yielding these films very conductive. It is for this reason that it was necessary to apply quite high values of current in order to observe a longitudinal voltage drop to access the intrinsic device impedance. A 2-terminal measurement will not suffice to extract the intrinsic material properties, which are limited and dominated by the contact resistances.
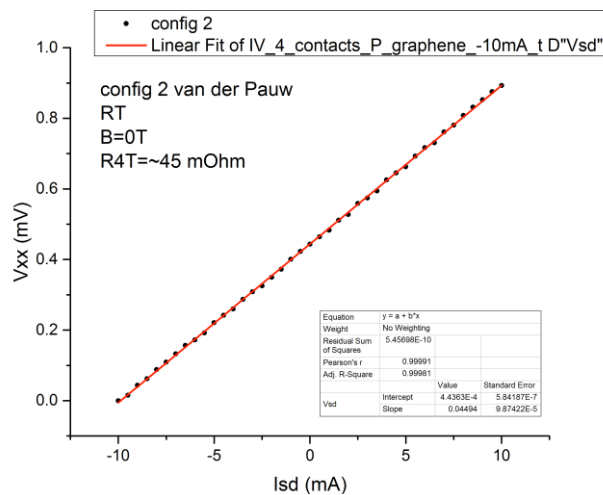
Fig 43. Current-voltage (IV) curve of the P-doped graphene material on HOPG taken at RT in zero magnetic field. The IV is linear and thus allows us to extract the intrinsic material resistance of Rxx=45 mΩ. Note the slight offset in the Vxx at 0 mA current, which is attributed to either our voltage pre-amplifier or the electronic setup, however does not affect the value of the slope. Since we do not know the thickness of the conductor(s), we cannot extract a

volumetric (bulk) resistivity, but rather work with a sheet resistance (square resistance in case of only 1 square, which is the case for a van der Pauw setup typically).

Next, we have used room temperature electromagnets to produce a DC magnetic field perpendicular to the film. The van der Pauw contact geometry is then switched from resistivity configuration to a Hall voltage probe configuration where a DC current (Isd) is send diagonally through the film and the transverse Hall voltage Vxy is detected by our voltage pre-amplifier (SR-560). Two different methods are then used to find the carrier density and mobility in this material.

In the first method (symmetrization), we apply a DC magnetic field in positive direction (+0.7 T) and record Vxy vs Isd over a 10 mA range. We then reverse the magnetic field and repeat the measurement. Then we take the average of the 2 data sets to filter out non-Hall related voltages and are hopefully left with the 'real' Hall voltage that results from the magnetic field only.

In the second method we apply a constant Isd current of 10 mA and step the field from -0.7 T to +0.7 T and record the Vxy values at each point of the magnetic field. The Rxy vs B curve should be linear and from its slope we can directly extract a 2D carrier density and mobility once the sheet resistance is known (from Fig. 43). The mobility (thickness independent quantity) can be calculated by taking the inverse of the product of electron charge, n2D and the sheet resistance.

As mentioned above, these two methods should reveal essentially the same information. However, in this case they do not. We start with the symmetrization results first.
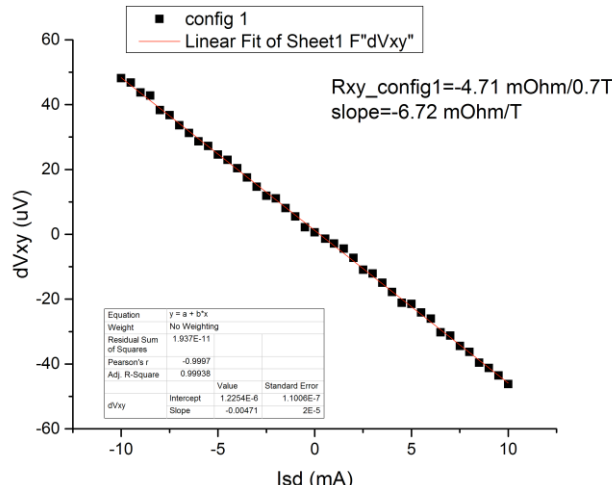

Fig 44. Symmetrized IV measurement. The resulting signal dVxy is obtained by subtracting the common voltage offset at positive and negative magnetic field, i.e.: dVxy(Isd) = 0.5*[Vxy(+B) - Vxy(-B)].

The resulting slope is a measure of the Hall resistance Rxy=Vxy/Isd for the fixed magnetic field applied (0.7 T) and can be used to calculate the Hall slope. Here we extracted a Hall slope of -6 mΩ/T. This results in a n$_{2D}$ value of ~6x10^{17} /cm^2. Repeated measurements like these have also shown Hall slopes of 1 mΩ/T, corresponding to a 2D carrier density n$_{2D}$ of 1x10^{17} /cm^2. Assuming these values of n$_{2D}$, one can then directly calculate the mobility of the carriers using the value of the sheet resistance R$_s$=45 mΩ (see Fig. 43). The mobility extracted μ=1/(n$_{2D}$*e*slope) varies between 200 and 1500 cm^2/Vs for the Hall slopes given above.

Next, we discuss the second method used to extract the Hall slope and compute carrier density and mobility values. Here a fixed current is applied through the film and the Hall voltage is directly recorded as a function of the magnetic field applied to the sample from negative to positive polarity.

In Fig. 45 we plot the Hall voltage vs. magnetic field taken at a DC current of 10 mA.
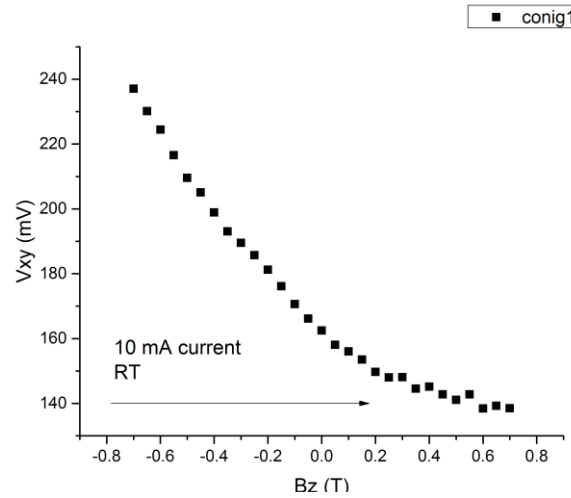

Fig 45. V_{xy} vs magnetic field taken at a constant current of 10 mA. The V_{xy} data is not anti-symmetric (but rather non-linear) with respect to the magnetic field. The up and down sweep of magnetic field produces the same result, so there is no hysteresis involved.

The data in Fig. 45 illustrates a highly non-linear Hall response, which is in contrast to the symmetrization data of Fig. 44. We have not understood this lack of consistency between these two methods.
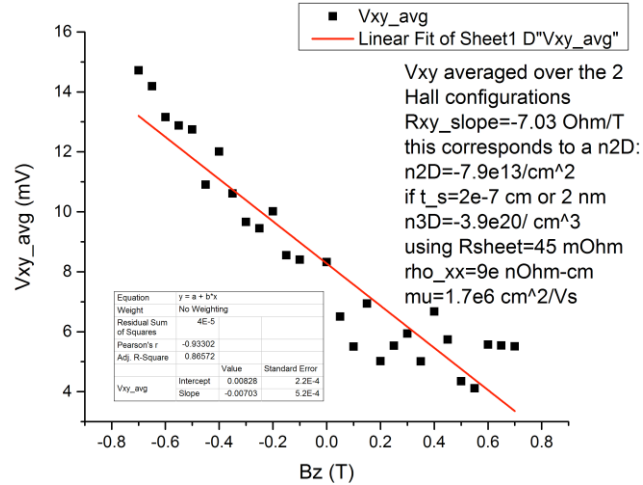

Fig 46. V_{xy} (averaged over the 2 Hall configurations) vs magnetic field taken at a constant current of 1 mA. The Vxy data is NOT as anti-symmetric with respect to the magnetic field as compared to the data in Fig. 45. By linear fitting we extract a Hall slope of ~ -7 Ω/T, which corresponds to a n_{2D} of about 8×10^{13} /cm^2 electrons. This value does NOT agree with the carrier density extracted by the symmetrization method as shown in Fig. 44. The slope is off by 3 orders of magnitude and therefore we cannot trust the data until we sorted out what is going on in each of the 2 methods.

There are several open questions regarding the characterization of the material by magnetic field. The sheet resistance is the only parameter that can be extracted with certainty. It seems that the DC current through the film also affects the value of the 4-terminal resistance itself, so there must be some kind of heating affect occurring in the device, which affects the carrier density and explains the difference

between data in Figs. 45 and 46.

Finally, we have looked at what happens with the material as a function of the temperature. We have used the symmetrization method to extract the Hall slope at liquid nitrogen (LN$_2$) temperature. The Hall slope value is virtually unchanged between RT and LN$_2$, which could indicate a semi-metallic behavior similar to the buried graphitic layer in ion-implanted diamond, which shows NO temperature dependence in the sheet resistance at all, even down to mK temperatures.
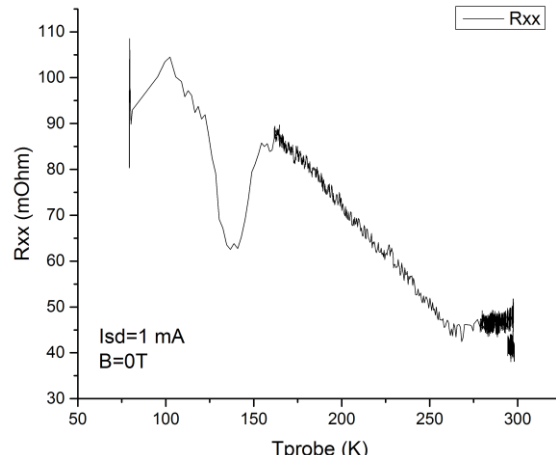

Fig 47. Temperature dependence of the film resistance for Isd=1mA and no applied magnetic field. A dip appears in the data around 150 K and a peak feature just above 100 K. At the end of the cooldown from RT to LN2 temperatures, the device resistance has more than doubled.

Figure 47 displays the resistance of the film measured as a function of time (temperature) for a bias of 1 mA and no applied magnetic field. More measurements have to be done varying parameters such as the applied magnetic field, DC current, etc. to find out if temperature drifts do not compromise the reliability of the data. Repeated measurements showed that this dip is not easily reproduced, which could indicate very sensitive temperature dependence of the material. We are therefore planning to record Hall data by (B-sweeps) at designated temperature points during a cool down (and a warm up) where sufficient time is given to let the material equilibrate before a measurement point is collected.

In order to provide some clarity to these anomalies we have sourced new samples, which are both doped and undoped. At the very least comparison of these two sample types should establish if the anomalies are related to P doping.

[6] Electrical characterization of the buried graphitic layer (He implanted) using a LN$_2$ Hall setup

We have continued to investigate the electrical properties of a buried graphitic layer formed by RT ion-implantation (in house) of He at 1.789 MeV energy with a fluence of ~5x10^{16} He/cm^2. The diamond plate was then annealed in vacuum at 1100°C for 1 hour. Cross-sectional TEM images have shown a buried graphitic layer that has a thickness of ~200-300 nm at a depth of ~ 1.6 um.

As previously reported, we have succeeded to create electrical contacts on this diamond plate using the laser cutter and using active braze alloy to fill up the holes. We then placed this sample in the Hall system for carrier density measurements using field sweeps at constant current of 10 mA.
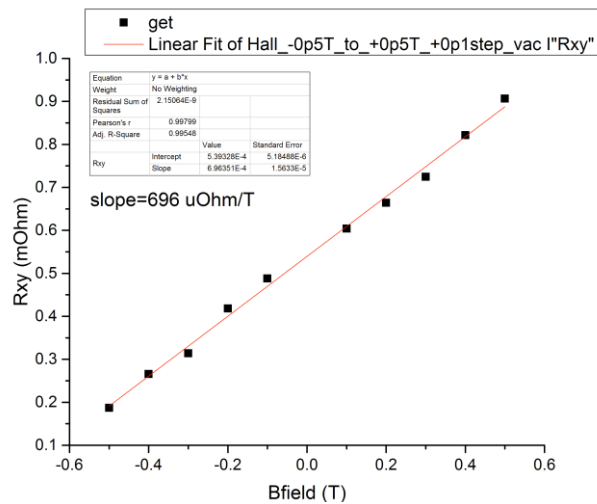
Fig 48. B-sweep response of the buried graphitic sample created by RT He-implantation (5x10^{16} He/cm^2) followed by HT annealing at 1100°C for 1 hour in vacuum.

The Hall slope corresponds to a value of ~0.7 mΩ-cm and n$_{2D}$=8.9x10^{17} /cm^2. Assuming that the thickness for this graphitic layer is 200 nm we extract a RT value of n$_{3D}$=4.45x10^{22} /cm^3. From van der Pauw measurements we have extracted a RT value of ρ_{xx}=2 mΩ-cm and a mobility value of μ =0.069 cm^2/Vs. These data imply that the carrier density in the graphitic material is enormous (carbon density equals 1.75x10^{23} /cm^3) and that it is very conductive indeed. However, using the Hall system we are still able to extract a Hall response.
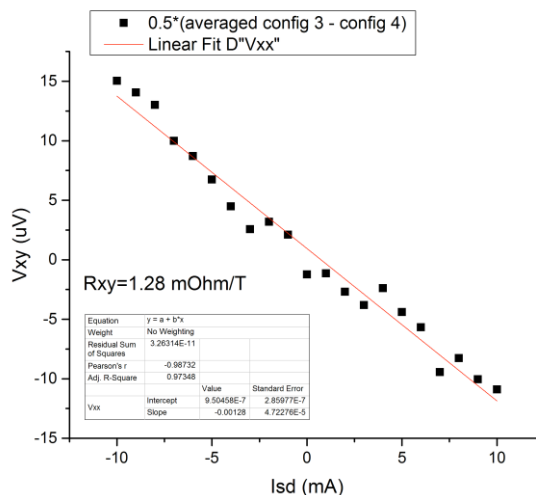
Fig 49. Symmetrized Hall data at RT of the buried graphitic sample for comparison.

We have also compared these B-swept data by taking Hall data using symmetrization. For this we swept the current from -10 to +10 mA at both +0.5 and -0.5 T magnetic field values. We find a Hall slope of ~1.28 mΩ/T, which is slightly larger as compared to the B-sweep data at constant current. The n2D extracted for this material using this method equals $n_{2D}=4.8\text{x}10^{17}$/cm^2. This is within a factor 2 the same as the value extracted by field sweeping (Fig. 48).

Conclusions:

In the optional funding research period we have:

- Hot-implanted (to avoid graphitization) diamond CVD grown plates with 2 MeV B atoms
- Performed optical and Raman spectroscopy of these samples before and after HTA
- Measured the $2x10^{16}$ B/cm^2 – 600°C IV at RT and its T-dependence (freeze out)
- Extracted at RT its carrier density using the Hall effect (density << MIT)
- Created a $1x10^{17}$ B/cm^2 – 600°C sample and characterized vs. temperature
- Extracted at 3-4 K its carrier density using the Hall effect (density < MIT)
- AFM analysis on the B-NCD material from Cardiff and measured its superconductivity
- We have measured P-doped graphene on HOPG samples vs. T and B-field + Raman analysis
- Characterized CVD grown B-doped single crystal diamond produced in reactors at MC^N

We conclude that we have introduced a very high amount of B in diamond plates by hot-implantation. We conclude that the diamond crystal lattice after HTA is as good as unimplanted diamond, which is very promising for increasing the boron concentration to even higher values (density > MIT). We have not observed a superconducting phase transition down to 120 mK for the highest B doped diamond sample, but have good evidence that we are nearing the MIT point, based on the resistance vs. temperature data of the $2x10^{16}$ B/cm^2 and the $1x10^{17}$ B/cm^2 – 600°C samples.

This technology will ultimately (once we have established a hole density above the MIT) allow the formation of buried conducing layers, which can be used at mK temperatures and put to use as gate electrodes for electronic devices in the diamond cap (think NV$^-$ centers) or on the surface (think hydrogen H-terminated diamond transistors). This would then allow electric field control of the surface carrier density without the need of depositing a gate dielectric and electrode from the topside.

It would also allow to control the magnetic flux in the vicinity of NV$^-$ centers (by sending DC currents through this buried layer), that can be used a very sensitive magnetometers. This will result in monolithic, robust device architectures useful for metrology purposes and sensing applications. For that purpose it might be better to reduce the distance from the surface to the buried layer as it will increase the capacitive coupling, but the dielectric constant of the diamond needs to be taken into account as well. All this assumes the implanted (HTA) diamond cap retains electrically insulating.

Future plans:

In order to observe superconductivity in boron-implanted diamond crystals we most likely need to increase the concentration of boron to values above the metal-insulator-transition and at the same time eliminate electronic trap states in the diamond layer that result from the ion-implantation process.

To tackle these issues, we will:

- Hot-implant single crystal diamond (600°C) at 1 MeV with fluences > $1x10^{17}$ B/cm^2
- Perform high pressure high temperature (HPHT) annealing to remove electronic damage
- Perform SIMS study to investigate the B doping profile and compare with Hall data
- Implement a gate electrode on top of the diamond cap to tune the carrier density in-situ
- Use the buried layer as a gate electrode for NV$^-$ centres in the diamond cap layer

An interesting idea for future devices is to use a gate electrode on the insulating diamond cap to induce more carriers into the buried layer and induce a metal-insulator-transition or even a superconducting transition when the carrier density exceeds the critical threshold. Measurements with devices as such can also reveal the dielectric strength of the recovered diamond cap.

List of Publications that resulted from AOARD supported project:

[1] OzCarbon 2013 conference: '*Raman analysis of boron-implanted diamond and subsequent high-temperature annealing – a route towards high-T_c superconductivity?*', L.H. Willems van Beveren, K. Ganesan, B.C. Johnson, A. Stacey, B.A. Fairchild, J.C. McCallum, M.L. Cohen, and S. Prawer, submitted abstract to the Australian conference on carbon based materials (OzCarbon), December 1-3, 2013.

[2] ICONN/ACMM 2014 conference: '*Raman analysis of boron-implanted diamond and subsequent high-temperature annealing*', L.H. Willems van Beveren, K. Ganesan, B.C. Johnson, A. Stacey, B.A. Fairchild, J.C. McCallum, M.L. Cohen, and S. Prawer, submitted abstract to the International Conference on Nanoscience and Nanotechnology (ICONN), February 2-6, 2014.

[3] COMMAD 2014 conference: '*Indium tin oxide film characterization using the classical Hall effect*', L.H. Willems van Beveren, E. Panchenko, N. Anachi, L. Hyde, D. Smith, T.D. James, A. Roberts and J.C. McCallum, submitted abstract to the International Conference on Optoelectronic and Microelectronic Materials and Devices (COMMAD), December 14-17, 2014.

Attachments:

Conference proceedings listed above.

References:

[1] 'Constraints on *Tc* for superconductivity in heavily boron-doped diamond', J.E. Moussa, and M.L. Cohen, *Physical Review B* **77**, p064518 (2008).

[2] 'Superconducting properties of homoepitaxial CVD diamond', Y. Takano, T. Takenouchi, S. Ishii, S. Ueda, T. Okutsu, I. Sakaguchi, H. Umezawa, H. Kawarada, and M. Tachiki, *Diamond & Related Materials* **16**, p911–914 (2007); 'Superconductivity in CVD diamond films', Y. Takano, *J. Phys.: Condensed Matter* **21**, p253201 (2009).

[3] 'Metal-insulator transition in boron-ion-implanted diamond', T. Tshepe, C. Kasl, J.F. Prins, and M.J.R. Hoch, *Physical Review B* **70**, p245107 (2004).

[4] 'Metal-insulator transition and superconductivity in boron-doped diamond', T. Klein, P. Achatz, J. Kacmarcik, C. Marcenat, F. Gustafsson, J. Marcus, E. Bustarret, J. Pernot, F. Omnes, Bo E. Sernelius, C. Persson, A. Ferreira da Silva, and C. Cytermann, *Physical Review B* **75**, p165313 (2004).

[5] 'Mechanism for the amorphisation of diamond', B.A. Fairchild, S. Rubanov, D.W.M. Lau, M. Robinson, I. Suarez-Martinez, N. Marks, A.D. Greentree, D. McCulloch, and S. Prawer, *Advanced Materials* **24**, p2024 (2012).

[6] 'The stopping and range of ions in solids', J. Zeigler, J.P. Biersack, and U. Littmark, Pergamon, New York, (1985).

[7] 'Diamond doped by hot ion implantation', N. Tsubouchi, M. Ogura, H. Watanabe, A. Chayahara, and H. Okushi, *Materials Science Forum* **600-603**, p1353-1356 (2009).

[8] 'Low-resistance p^+ layer formation into diamond using heavily B ion implantation', N. Tsubouchi, M. Ogura, Y. Horino, and H. Okushi, et al, *Applied Physics Letters* **89**, p012101 1-3 (2006).

[9] '*p*-type doping by B ion implantation into diamond at elevated temperatures', N. Tsubouchi, M. Ogura, H. Kato, S.G. Ri, H. Watanabe, Y. Horino, and H. Okushi, *Diamond & Related Materials* **15**, p157-159 (2006).

[10] 'Absence of superconductivity in boron-implanted diamond', V. Heera, R. Höhne, O. Ignatchik, H. Reuther, and P. Esquinazi, *Diamond & Related Materials* **17**, p383–389 (2008).

[11] 'Raman investigation of damage caused by deep ion implantation in diamond, J.O. Orwa, K.W. Nugent, D.N. Jamieson, and S. Prawer, *Physical Review B* **62**, p5461-5472 (2000).

[12] 'Formation of buried *p*-type conducting layers in diamond', R. Walker, S. Prawer, D.N. Jamieson, and K.W. Nugent, R. Kalish, *Applied Physics Letters* **71**, p1492-1494 (1997).

[13] 'Raman scattering from MeV-ion implanted diamond', J.D. Hunn, S.P. WIthrow, and C.W. White, D.M. Henbree, Jr., *Physical Review B* **52**, p8106-8111 (1995).

[14] 'Superconductivity in diamond thin films well above liquid helium temperature', Y. Takano, M. Nagao, I. Sakaguchi, M. Tachiki, T. Hatano, K. Kobayashi, H. Umezawa, H. Kawarada, *Applied Physics Letters* **85**, p2851-2853 (2004).

[15] 'Optical and electronic properties of heavily boron-doped homo-epitaxial diamond', E. Bustarret, E. Gheeraert, K. Watanabe, *phys. stat sol. (a)* **199**, p9-18 (2003).

[16] 'Dependence of the superconducting transition temperature on the doping level in single-crystalline diamond films', E. Bustarret, J. Kačmarčik, C. Marcenat, E. Gheeraert, C. Cytermann, J. Marcus, T. Klein, *Physical Review* Letters **93**, p237005 1-4 (2004).

[17] 'Ion-beam-induced transformation of diamond', S. Prawer, and R. Kalish, *Physical Review B* **51** p15711-15722 (1995).

[18] 'Graphitization of diamond by ion impact: Fundamentals and applications', R. Kalish, and S. Prawer, *Nuclear Instruments and Methods in Physics Research Section B: Beam Interactions with Materials and Atoms* **106**, p492-499 (1995).

[19] 'Formation of delta-doped, buried conducting layers in diamond, by high-energy, B-ion implantation', C. Uzan-Saguy, R. Kalish, R. Walker, D.N. Jamieson, and S. Prawer, *Diamond & Related Materials* **7**, p1429-1432 (1998).

[20] 'Superconductivity and low temperature electrical transport in B-doped CVD nanocrystalline diamond', M. Nesládek, J.J. Mares, D. Tromson, C. Mera, P. Bergonzo, P. Hubik, J. Kristofik, *Science and Technology of Advanced Materials* **7**, S41-S44, (2006).

[21] 'Growth and properties of nanocrystalline diamond films', O.A. Williams and M. Nesládek, *phys. stat sol. (a)* **203**, p3375-3386 (2006).

[22] 'Metal-insulator transition and superconductivity in boron-doped diamond', T. Klein, P. Achatz, J. Kacmarcik, C. Marcenat, F. Gustafsson, J. Marcus, E. Bustarret, J. Pernot, F. Omnes, Bo E. Sernelius, C. Persson, A. Ferreira da Silva, and C. Cytermann, *Physical Review B* **75** p165313 1-7 (2007).

[23] 'Transport behaviour of boron delta-doped diamond', J. Scharpf, A. Denisenko, C. I. Pakes, S. Rubanov, A. Bergmaier, G. Dollinger, C. Pietzka, and E. Kohn, *phys. stat sol. (a)* **210**, p2028-2034 (2013).

[24] 'Can doping graphite trigger room temperature superconductivity? Evidence for granular high-temperature superconductivity in water-treated graphite powder', T. Scheike, W. Böhlmann, P. Esquinazi, J. Barzola-Quiquia, A. Ballestar, and A. Setzer, *Advanced Materials* **2012**, p1-4, (2012); 'Granular superconductivity at room temperature in bulk highly oriented pyrolytic graphite samples', T. Scheike, P. Esquinazi, A. Setzer, W. Böhlmann, *Carbon* **59**, p140-149 (2013).

Appendix:

Here we discuss the experimental results that are of secondary importance and not primarily related to this project, but are worth nevertheless to disclose.

[7] Hydrogen implanted diamond followed by HPHT anneal to create shallow graphitic layers

[8] Hall and resistivity measurements on B-doped CVD grown single crystal diamond (MC^N)

[7] Hydrogen implanted diamond followed by HPHT anneal to create shallow graphitic layers

We have in parallel looked at the possibility to investigate the electrical properties of shallow graphitic layers in DC6 diamond formed by RT low-fluence (5.1 / 5.9 and 4.3×10^{16} H_2^+/cm^2) ion-implantation of hydrogen at 25 keV energy. These samples were post implantation high-pressure high-temperature annealed (HPHT) at 1200°C under 5 GPa pressure. The buried layers formed are typically ~20-50 nm thick and are buried only < 200 nm below the diamond surface (X-TEM analysis). These samples are potentially interesting because H-doped graphite has been reported to show magnetic properties. We can therefore expect a similar phenomenon in these samples.
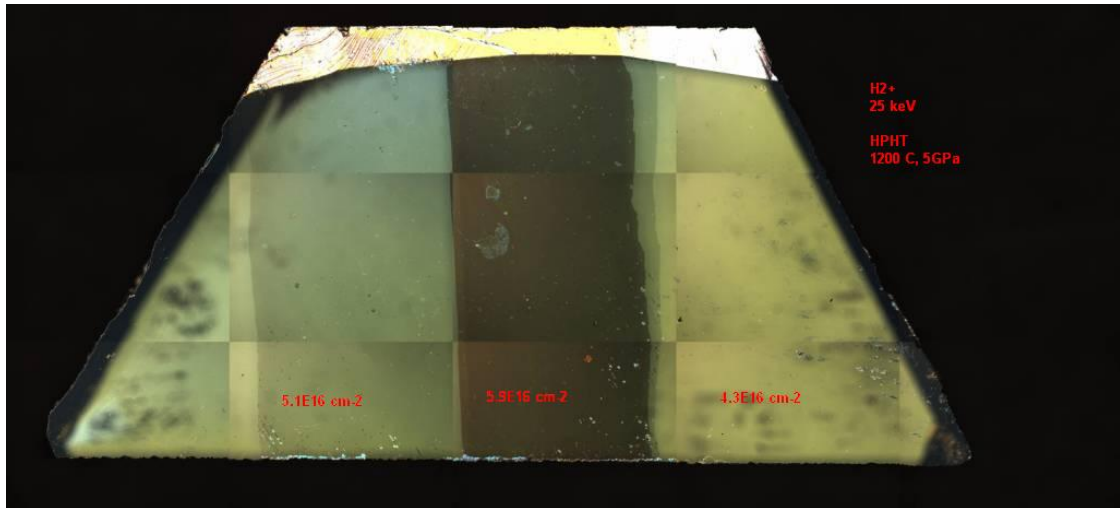

Fig 50. Optical microscopy image of electrical contacts to the H_2^+ implanted sample.

In Fig. 50 we show a top-lit optical microscope image of the H_2^+ implanted sample. The most left part of the diamond plate was left intentionally un-implanted (pristine). Raman spectroscopy was performed on these layers (by collaborators) as shown in Fig. 51. In black the Raman spectrum taken with a 325 nm laser of the undoped (pristine) DC6 diamond. Cyan, green and pink show the spectra for increasing fluence. Evident is the appearance of a G peak around 1500-1600 /cm for the implanted regions. This signal agrees with a RT ion-implantation above the graphitization limit. Furthermore; we see a quenching of the band around 2200-2600 /cm for the highest fluence sample.
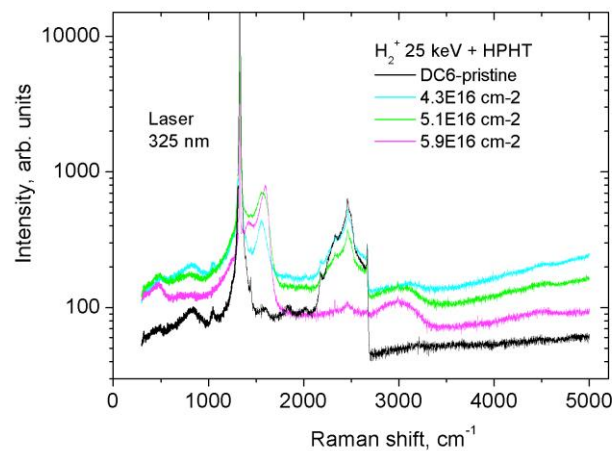

Fig 51. Raman spectroscopy of the H_2^+-implanted diamond plate after HPHT annealing.

We have succeeded to create electrical contacts on the diamond plate using laser cutter and brazing techniques. To maximize the yield of sample 'real estate' to measure in the implanted regions, we have adopted a new methodology, i.e. carve out a 2D matrix of holes all over the sample followed by contact brazing. These contacts will allow us to measure in a van der Pauw / Hall arrangement multiple sections of the implanted regions. This allows for statistical analysis, which can tell us e.g. if the doping across the sample is uniform or not.
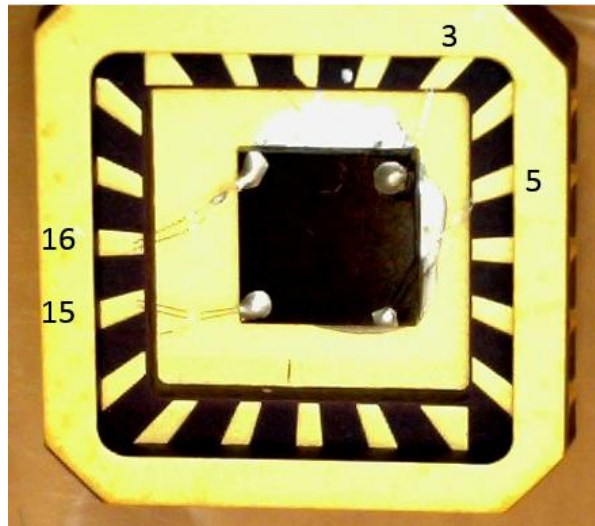
In addition, using the Hall system, we can map out as a function of temperature how the different regions responds to a cooldown. By plotting the logarithm of the resistivity (mobility and density) vs. 1000/T we might find out if variable range hopping or other transport mechanisms (dielectric regime) dominate the electronic transport. Since this material is most likely graphitic in nature (RT ion-implantation above the critical dose creates a graphitic layer as evidenced by Raman spectroscopy), we expect a very high carrier density in a layer just below the diamond cap.

Fig 52. Optical microscopy image of electrical contacts to the H_2^+ implanted sample.

In Fig. 52 we can see the electrical contacts to the H_2^+ implanted sample. We made several contacts in each of the different fluence implanted area's to maximize area of the sample that can be used for the measurement infrastructures. The different colors represent areas with different ion implantation density. There are 4 different areas visible with each their distinct color. From left to right these regions correspond to a doping density of: 0 / 5.1 / 5.9 / 4.3 and $5x10^{16}$ H_2^+ /cm^2, from left to right respectively. The pink region in the middle has the highest doping. The sample is currently mounted in a chip carrier ready for wire bonding. There are many contacts to each region allowing for van der Pauw / Hall as well as 4-point probe (linear) measurements.

[8] Hall and resistivity measurements on B-doped CVD grown single crystal diamond (MC^N)

We have started to grow single-crystal B-doped diamond films in the new CVD reactors of the MC^N. The 1st sample was characterized at RT by symmetrization with a permanent magnet to establish a carrier density. It was then cooled down and showed a strong increase in resistance, which seems to indicate the sample is doped below the MIT. A 2nd sample shows a much lower resistance, but has not been cooled down yet to establish whether there is a carrier freeze out or a superconducting transition.

Fig 53. Image of the electrical contacts to the first MC^N-grown sample. The wire bonds were pushed down into a 2-component conducting silver paste, followed by curing at 150°C.

One can already see that the diamond density is not uniform throughout the plate as it appears lighter on the right side. This could be caused by the plasma being of different intensity during growth. Using a multimeter at RT we can measure the 2-terminal resistance between contacts, i.e. R_{2T}=4.4 kΩ in one configuration and R_{2T}=176 kΩ in the perpendicular configuration of a van der Pauw sample. The 4-terminal resistance of the sample in each configuration is R_{4T}=125 Ω and 144 Ω, respectively.

So one can conclude that the contact resistance is quite different between contacts, but that the intrinsic sample resistivity is still quite similar. The thickness of the B-doped film is estimated to be around 3 µm, which results in a volume resistivity of 40.5 mΩ-cm, assuming an averaged sheet resistance of 135 Ω. The estimated doping density of this sample would be 1×10^{17} /cm^3. The Hall data in Fig. 53 show that the carrier density extracted is indeed close to that value and $n_{3D} \sim 4\times10^{17}$ /cm^3. Note that for a superconducting transition in CVD-grown B-doped single crystal diamond a boron concentration of only 0.18% B is required, or a hole concentration of n_{3D}=9.4$\times10^{20}$ /cm^3 [14]. Other papers cite a value of n_{3D}=4.5$\times10^{20}$ /cm^3 [22].

Note that the first few data points around are slightly offset from the rest as the current switches suddenly from 0 to -10 µA and it takes a few seconds to establish a steady state of transport. After this, the up and down sweep show no hysteresis anymore.
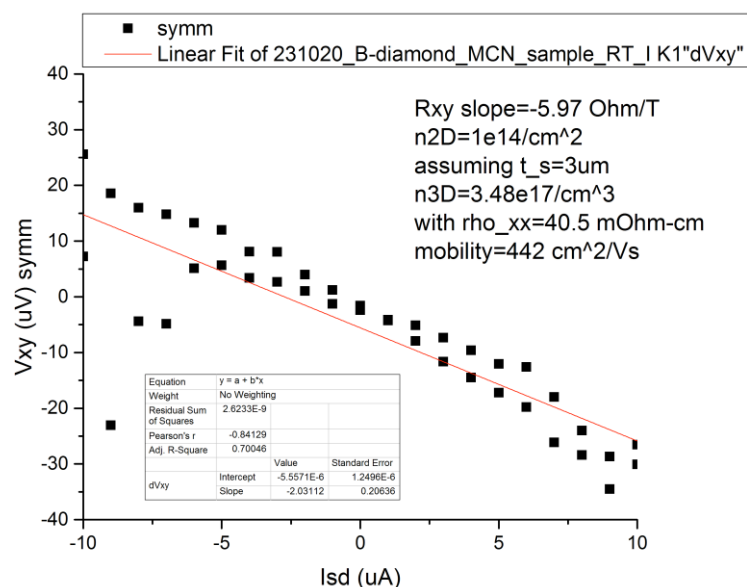
Fig 54. Hall data collected by symmetrization at RT illustrating a carrier density around $3x10^{17}$ /cm³. The material has a resistivity of ~40 mΩ-cm, assuming a thickness of 3 μm.

The 1st MC^N sample shows a resistance increase upon cooldown (Fig. 55). However, the sample socket used to hold the chip carrier lost contact around 108 K and a sudden step to compliance of the voltage pre-amplifier makes it impossible to extract further data. The measurement needs to be repeated down to lower temperatures to map out the resistance increase.
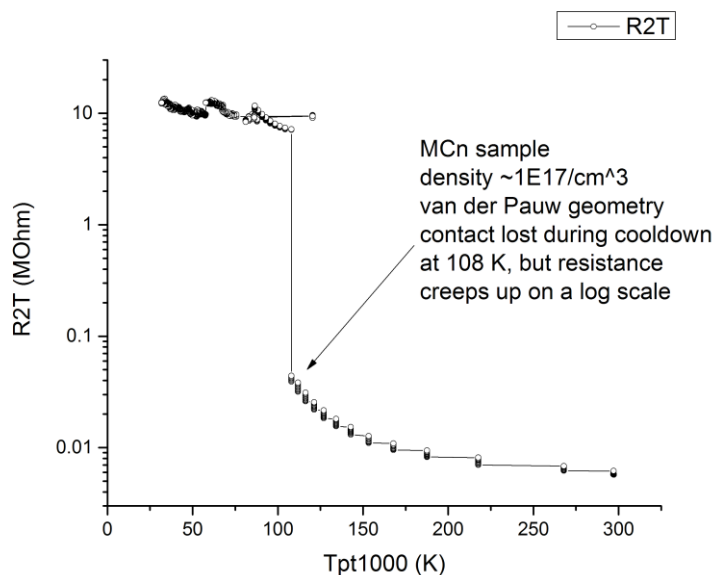

Fig 55. Resistance data of MC^N sample 1, collected as a function of temperature in a cool down of the probe. A sudden jump in R_{2T} around 108 K is caused by a faulty sample socket.

A 2nd sample from the MC^N was grown with a higher boron doping density. Unfortunately, there was not enough real estate available on the diamond plate to create a van der Pauw square. Instead, 4 contacts were created in series to perform a resistivity measurement, which could then be compared to the 1st grown MC^N sample, but this geometry won't allow carrier density extraction.

The 2nd MC^N sample has a much lower 2-terminal resistance between the contacts, i.e. R_{2T}=21 Ω (c.f. Fig. 56) and R_{4T}=1.58 Ω (c.f. Fig. 57). Both samples will need to be cooled down to see how their resistance changes with respect to another. Obviously, we expect the sample with the lower resistivity to be more resistant against carrier freeze out. This has also been observed for the diamonds that were hot-implanted. Ideally, we will find for which B concentration a superconducting transition occurs.
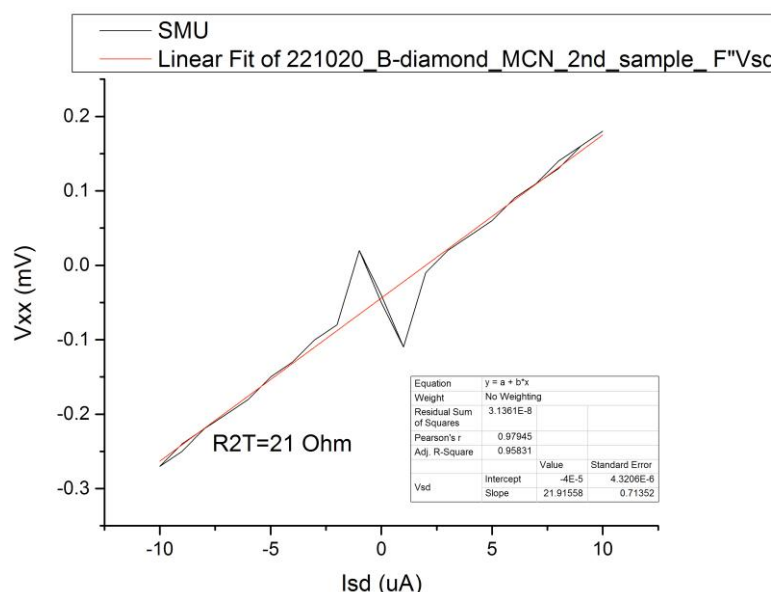

Fig 56. I-V data taken at RT of the 2nd MC^N sample. The material has a R_{2T}= 21 Ω. The spike at 0 µA is due to sourcing small currents with our source and is not sample-related.

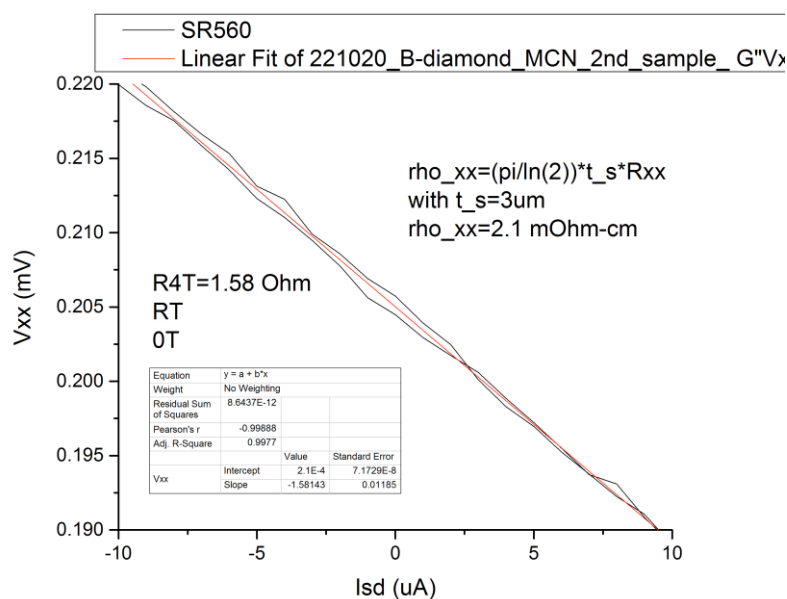*Fig 57. I-V data taken at RT of the 2nd MC^N sample. The material has a R_{4T}= 1.58 Ω.*

The resistivity of the material turns out to be $\rho_{xx} \sim 2.1$ mΩ-cm, assuming a thickness of 3 μm, which is which is an order of magnitude lower than the first MC^N sample. This implies that we are capable of increasing the carrier density by the CVD growth process and moving towards the direction of creating such high carrier densities so that the material does not freeze out at low temperatures, which could be a requirement for the observation of superconductivity in these materials.

Key for creating reliable samples is the uniformity of the plasma over the dimensions of the diamond plate. Also, it is essential to get rid of any impurities in the CVD chamber before a run takes place. We are currently optimizing the CVD process and expect to have highly-doped (boron) single crystal diamond plates very soon for further processing and subsequent measurements at low temperature.